



GISUP 2020, International

THE 22TH INTERNATIONAL SYMPOSIUM OF GEOSPATIAL INFORMATION SCIENCE AND URBAN PLANNING

November 28, 2020

Beijing University of Civil Engineering and Architecture,
Daxing District, Beijing China

Organizing Committee of GISUP2020, International



GISUP 2020, International

The 22th International Symposium of
Geospatial Information Science and Urban Planning

November 28, 2020

Beijing University of Civil Engineering and Architecture,

Daxing District, Beijing China

Organizing Committee of GISUP2020, International

Welcome to GISUP 2020



Dear colleagues:

We would like to thank the many participants in the 22nd International Symposium on Geospatial Information Science and Urban Planning (GISUP-2020) for their continued interest in the conference. Due to the influence of COVID-9, we have decided to move the conference to a virtual event held on November 28th, 2020 online. I am Professor Mingyi Du, President of the School of Geomatics and Urban Spatial Information, Beijing University of Civil Engineering and Architecture. Our school has been participating in GISUP every year since four years ago, witnessing the increasing scale of participation and academic improvement of this seminar. It is a high-level platform for scholars from east Asian countries and regions to exchange and communicate research achievements in geospatial information science and urban planning.

GISUP-2020 was to be held in Beijing, China. As the capital of China, Beijing is an ancient city with a history of five thousand years. Beijing is the capital of China, an ancient city with a history of five thousand years. Beijing is the center of China's political, cultural, scientific, educational and international exchanges. There are many places of interest in Beijing, such as the world's largest imperial palace-the Forbidden City, the temple of heaven, the imperial garden-Beihai Park, the Summer Palace and the Old Summer Palace, the Badaling Great Wall, the Mutianyu Great Wall and the world's largest quadrangle courtyard-Prince Gong Mansion.

We look forward to meeting you online during GISUP-2020.

Conference Chair, Prof. Mingyi DU

A handwritten signature in blue ink, which appears to read "杜明义" (Du Mingyi).

Published by

GISUP, INTERNATIONAL
1-14 Bunkyo-Machi, Nagasaki City, 852-8521, Japan

GISUP 2020, International

The 22nd International Symposium of Geospatial Information Science and Urban Planning

Copyright (c) 2020 by GISUP, INTERNATIONAL

All rights reserved. This book, or parts thereof, may not be reproduced in any form or by any means, electronic or mechanical, including photocopying, recording or any information storage and retrieval system now known or to be invented, without written permission from the Publisher.

ISBN: 978-4-9907633-6-7

Typeset by

Secretariat of Organizing Committee

office@gisup.org <http://gisup.org>

Printed by

Organizing Committee of GISUP2020

Organization Committee

Conference Chair:

Mingyi Du, Beijing University of Civil Engineering and Architecture, China
(dumingyi@bucea.edu.cn)

Vice Chair(China):

Xianglei Liu, Beijing University of Civil Engineering and Architecture, China
(liuxianglei@bucea.edu.cn)

Jian Wang, Beijing University of Civil Engineering and Architecture, China
(wangjian@bucea.edu.cn)

He Huang, Beijing University of Civil Engineering and Architecture, China
(huanghe@bucea.edu.cn)

Changfeng Jing, Beijing University of Civil Engineering and Architecture, China
(jingcf@bucea.edu.cn)

Vice Chair(Korea):

Kiyun Yu, Seoul National University, Korea
(kiyun@snu.ac.kr)

Vice Chair(Japan):

Rieko Nakao, Nagasaki University, Japan
(rieiko@nagasaki-u.ac.jp)

Vice Chair(Taiwan):

Cheng-Di Dong, National Kaohsiung University of Science and Technology, Taiwan
(cddong@nkust.edu.tw)

Members:

Jui-Chung Kao, National Kaohsiung University of Science and Technology, Taiwan
(jkao@wnkust.edu.tw)

Hui-Lun Yu, National Kaohsiung University of Science and Technology, Taiwan
(hlyu@nkust.edu.tw)

Ming Huang, Beijing University of Civil Engineering and Architecture, China
(huangming@bucea.edu.cn)

Liang Huo, Beijing University of Civil Engineering and Architecture, China
(huoliang@bucea.edu.cn)

Dean Luo, Beijing University of Civil Engineering and Architecture, China
(luodean@bucea.edu.cn)

Takeshi Yamaguchi, University of the Ryukyus, Japan
(t-yama@edu.u-ryukyu.ac.jp)

Takahito Ueno, Sojo University, Japan
(ueno@ed.sojo-u.ac.jp)

Chang-Hahk Hahm, Inha Technical College, Korea
(chhahm@inhate.ac.kr)

Eung-Nam Kim, Inha Technical College, Korea
(kimen@inhatec.ac.kr)

Won-Dae Kim, Inha Technical College, Korea
(kimwd@inhatec.ac.kr)

Dongha Lee, Kangwon National University, Korea

[\(geodesy@kangwon.ac.kr\)](mailto:geodesy@kangwon.ac.kr)

Atsuko Yasutake,Nagasaki University,Japan

[\(yasutake@nagasaki-u.ac.jp\)](mailto:yasutake@nagasaki-u.ac.jp)

Byungdug Jun,Nagasaki University,Japan

[\(bdjun@nagasaki-u.ac.jp\)](mailto:bdjun@nagasaki-u.ac.jp)

Catalog

• Welcome to GISUP 2020	I
• Organization Committee.....	III
• Online lectures to cope with Corona infection at Nagasaki University	2
• Multi-mode remote sensing collaborative monitoring and accurate detection of small and medium-span Bridges	7
• Producing DEM using Drone 3D Point Cloud.....	15
• Deformation Monitoring in Expressway Infrastructure Construction Using Drone.....	19
• Factors related to the “Ikigai” among elderly participating in community-based activities in Nagasaki, Japan.....	24
• Estimation of the Land Deformation Used by Sentinel-1A SAR Data Applied on Dangjin Reclaimed Area, Korea.....	28
• Analysis of Displacement Around Kumamoto Earthquake area Using InSAR Technology	34
• Edge Extraction Algorithm for Road Markings Based on Single-Frame Image and Sparse Point Cloud.....	42
• 3-D Model Reconstruction of Buildings by integrating Oblique Photography and Terrestrial LiDAR	56
• Development of Assistive Devices to Assist Daily Lives for People with Disability.....	69
• VR Contents Development for Peace Education Class with Flight Yoke System and Headset.....	75

Keynote Lecture

Online lectures to cope with Corona infection at Nagasaki University

Takakazu ISHIMATSU(ishi@nagasaki-u.ac.jp) Nagasaki University

Munenori SAKAI(m-sakai@nagasaki-u.ac.jp) Nagasaki University

Jiangli Yu(jiangli@gmail.com)Tamadic Co.Ltd

ABSTRACT: Corona virus issue is a serious social problem that we should overcome. The corona virus problem requires our social society to renew our living style. Education style in universities are now discussed to change new system using ICT technologies. Nagasaki University is trying to cope with this problem and to find new education system. In this paper we discuss how Nagasaki University

1. Introduction

Corona virus caused world-wide pandemic in this year.

Although in east Asian countries the situation is becoming a little bit better, the corona virus damages are still prevailing seriously in many countries. And we can't say when the infection will cease.

The corona virus caused serious damages in many aspects, economy, our daily lives, sport and music events and education. And it is required to change our living style to coexisting live with corona virus. What we have to consider most is the infection of corona virus by the human exchange in the society. People are required to wear mask, refrain from going out, avoid tight cluster of people. And patients of corona virus were quarantined.

In Nagasaki prefecture, the total number of corona infected patient is 251 people on 17th. Nov.

Governments and schools are trying to suppress the increase the infested patients.

In Nagasaki prefecture, the first infested patient was reported on 14th, March. After that the number of the infected patient increased gradually. In order to suppress the prevailing the corona virus, public school were closed during 4th/March till 24th/May and also 22nd/April till 10th/May. In the Nagasaki University more severe measures were adopted. Graduation ceremony, Entrance ceremony and also classes are closed.

All classes from April till August were requested to carry out on-line lectures.

Students were requested to study at home. Serious situation occurred to fresh students. Even they succeeded to enter university, opportunities to go to university and to enjoy the discussion with classmate were limited.

While every kinds of human activities were suppressed by the corona virus, ICT technologies offered effective measures. Nagasaki University had already innovated education system since 2012 and developed Learning Assessment & Communication System (LACS). The LACS is effective to cope with the new education style. In this innovation, various approaches were performed as follows:

- 1) Employment of learning management system developed at blackboard Co.Ltd in 2012.
- 2) All students were requested to
- 3) Information technology in the education was promoted
- 4) Employment of video distribution system.

In this presentation we describe how education in Nagasaki University could be carried out by the help of education system LACS.

2. Three type of on-line lecture

Since April/2020 we started three types of new education system as follows.

- 1) Real-time lecture to use web meeting system.
- 2) On-demand lecture to use video materials.
- 3) Web-lecture to use PDF materials.

These lectures can be readily accessible through Nagasaki University LACS(Learning Assessment & Communication System). And after the lectures students can submit the report through LACS.

In Fig.1 learning status of on-line lecture in the spring season is shown. As you notice, on-line lectures

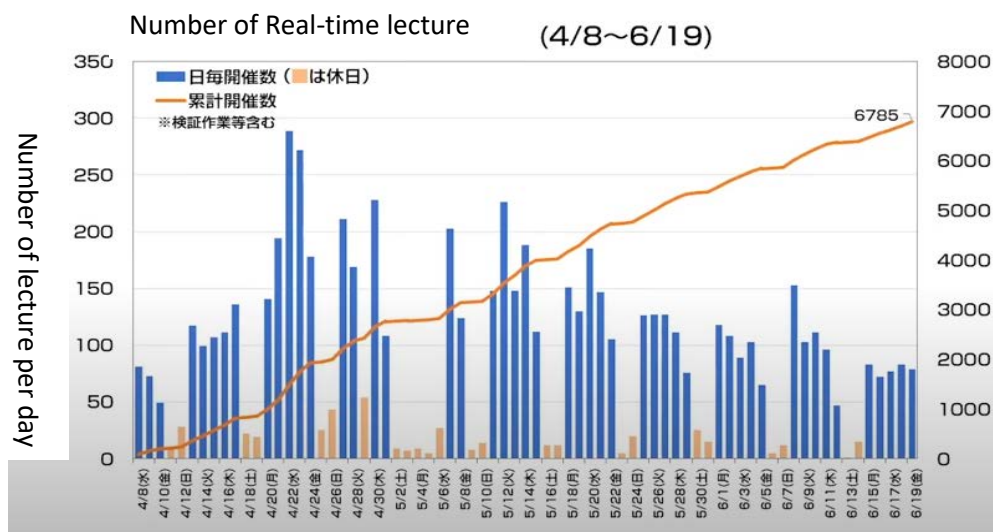


Fig.1 Number of real-time lectures between 8/April and 19/June

started from the 8th/April. And the accumulated number of real-time lectures amounts 6785 in June.

Web meeting system employed in Nagasaki University are

1. Blackboard Collaborate Ultra
2. ZOOM
3. Cisco Webex
4. Microsoft Teams

It was reported that

457 professors have used the on-line lectures.

6157 students studied the on-line lectures.

Totally 133,021 hours spent for on-line lectures.

In Fig.2 learning status of on-demand lecture in the spring season is shown.

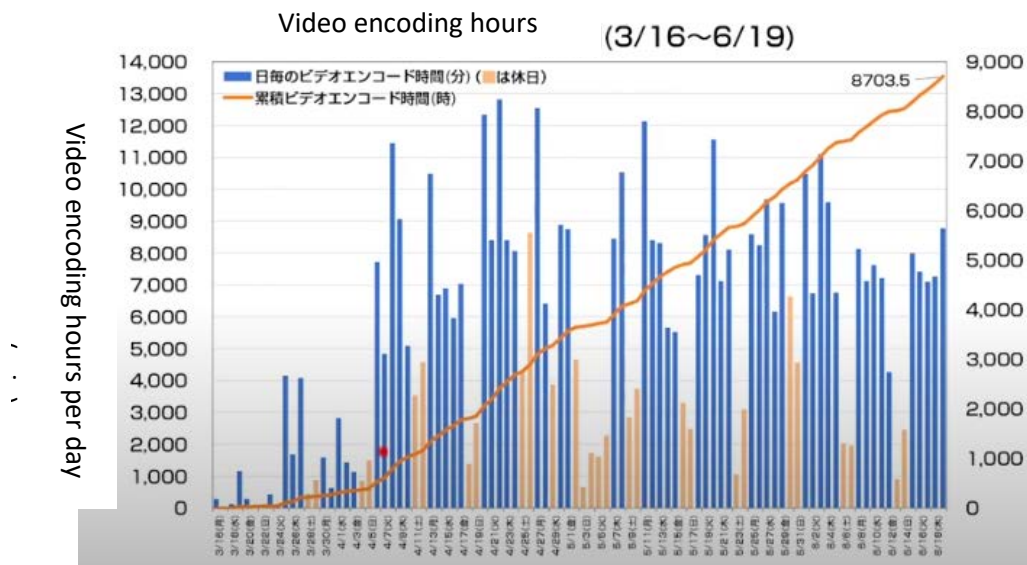


Fig.2 Video encoding hours for on-demand lectures between 16th/March and 19th/June

This figure shows video encoding time for the on-demand lectures.

It was reported that

Total number of video was 3200.

Total hours of encoding was 8,703 hours.

Total data transmitted to students was 29.9TB

3. Example of on-line lecture

On-line lectures named “Career exchange” is carried out in October and November. At every lecture a guest speaker is invited to talk with students. A distinguished feature of on-line lecture is that guest speakers can be selected in various fields and various areas as shown in the Table 1.

Table 1 Contents of on-lien lecture “Career exchange”

1) Diet member in NIIGATA pref.	2)Director of news media in Tokyo
3)President of Company in Saitama pref.	4)Curator of ancient era in Osaka
5)Dentist in Nagasaki pref.	5) Active patient with serious disability in Nagasaki
7)Director of insurance Co. in Tokyo	8) Street performer in Nagasaki
9) Audio engineer in Hollywood	10) Engineer to develop Shinkansen from Gifu pref.
11)Movie director in Tokyo	12) Director of Manufacturing Co. in Tokyo

In the lecture speakers and students could enjoy discussions together. Video image of on-line lectures are shown in Fig.3.

As a second example of on-demand lecture, the content of the “Nagasaki Story” is shown briefly in Table2. Total number of students are 1600 persons. Last year students are divided to seven classes since seating capacity of class rooms are limited. But in case of on-demand lecture, the number of students of the class is free from limitation. Therefore, I proposed to students to select speakers as she or he wants. Because of the introduction of freedom to select speakers, students could study the subjects more eagerly.

Table 2 Contents of on-demand lecture “Nagasaki story”

Opening	Title	Remarks
2 nd	Nagasaki and Christian	Two speakers (foreigner and Japanese)
3rd	Nagasaki life in international voyage era	Two speakers
4rd	Nagasaki and atomic bomb	Two speakers(male and female)
5rd	Nagasaki news	Three speakers from media
6rd	About active living	Six speakers
7rd	About active living	Six speakers
8rd	About active living	Six speakers



Fig.3 Video clip from "Career exchange"

4. Discussions

In Nagasaki University, on-line lecture and on-demand lecture could be carried out by the innovation of education system since 1992. Experience of the new style education revealed the following remarks.

- 1) On-line and on-demand lecture offer new education style. We can be free from area. We can discuss peoples in far place although we are close. It is like a magic. We don't need long travelling time to meet peoples in Korea and China. This feature to connect peoples in various areas.
- 2) One problem to on-line and on-demand lecture is that infrastructures to support efficient lectures are not sufficient. Once we try to download and upload video-image data, we often have to wait 30minutes and one hour. Furthermore, internet environment of students are often too weak. We hope advanced internet environment should be implemented sooner.
- 3) Some professors are skillful at using new education system. Of course, some professors hesitate to use such new education system. And some of them have an opinion that conventional lectures are more effective as education measures. I believe that on-line lecture and on-demand lecture is renovating our society to next fruitful one. Conventional lecture, on-line lecture and also on-demand lecture have advantageous point respectively. We should accept each advantageous point.

Multi-mode remote sensing collaborative monitoring and accurate detection of small and medium-span Bridges

Xianglei Liu, Yimeng Huang

Key Laboratory for Urban Geomatics of National Administration of Surveying, Mapping and Geoinformation, Beijing University of Civil Engineering and Architecture, Zhanlanguan Road, Beijing 100044, P. R. China

Abstract: As an important hub of traffic foundation, the safety of bridge plays an important role in national economy and property safety. At present, the dynamic monitoring and safety assessment of bridge has always been a hot issue in society. In this paper, the key technologies of collaborative monitoring and precise flaw detection integrating TLS, GBSAR and PSP-InSAR are developed. Firstly, TLS technology is used to obtain the point cloud data of the lower surface of the bridge, and the bridge surface model is constructed to analyze the potential damage area of the bridge; secondly, use GBSAR to obtain bridge dynamic deflection information, construct a W-ESMD two-stage noise reduction model integrating multi-wavelet threshold denoising and Extreme-point Symmetry Modal Decomposition (ESMD) methods and an Essen-Froome atmospheric parameter optimization and correction model that takes into account microwave transmission distance, targeted reduce signal noise, improve monitoring data accuracy, and propose damage identification methods based on the instantaneous frequency and instantaneous total energy; Finally, the PSP-InSAR method is introduced to realize the accurate judgment of the cause of bridge damage.

Key words: Ground Based Synthetic Aperture Radar; Precision Flaw Detection; Dynamic Monitoring;

0 Introduction

As an important hub of traffic foundation, the safety of bridge plays an important role in national economy and property safety. Under the influence of traffic congestion, vehicle overload, surrounding environment, geological activities and other coupling factors, the bridge operation safety risk increases significantly, ranging from serious disease to rapid aging, even sudden collapse [1]. Therefore, in order to ensure the safety performance of bridges, it is necessary to carry out dynamic monitoring and safety assessment of bridges.

The Terrestrial Laser Scanning (TLS) technology has the advantages of multiple data points, large data volume, and non-contact. By acquiring point cloud data on the bridge surface and constructing a three-dimensional deformation field on the bridge surface, the periodic deformation analysis can be performed, accurately obtain static deformation data of the bridge surface [2]; Ground Based Synthetic Aperture Radar (GB-SAR) interferometry technology is a new technology that integrates the advantages of synthetic aperture radar and interferometry that has emerged in recent years. It has the advantages of non-contact, high precision (0.01mm), high sampling frequency (1000Hz) and overall dynamic monitoring [3]. This technology can solve many problems of traditional deformation monitoring technology, such as small measurement range, short measurement distance, low accuracy, and environmental impact, and has been widely used in bridge dynamic characteristics monitoring [4]; The PSP-InSAR technology developed by synthetic aperture radar interferometry (InSAR) technology can construct a PS grid expansion algorithm that connects pixel pairs with the same phase characteristics and a bridge damage analysis method based on the relative deformation rate and relative elevation difference between the PS pairs, and realize accurate microscopic judgment of the cause of bridge damage [5,6].

Therefore, this paper adopts the key technologies of integrating TLS, GB-SAR and PSP-InSAR to provide technical support for the collaborative monitoring and precise flaw detection of small and medium-span bridges. This has important theoretical significance and application value for ensuring the healthy operation of small and medium-span bridges and reducing the cost of inspection and maintenance of the health of small and medium-span bridges.

1 Potential damage detection of small and medium-span bridges using TLS

According to the characteristics and advantages of the 3D laser scanner, this research uses the 3D laser scanner to monitor the deformation of the small and medium-span bridges to obtain the specific deformation area.

1.1 Automatic registration of point cloud data based on line features

① Point cloud data segmentation

The RANSAC method is the most commonly used method of point cloud data segmentation based on surface features. It has the characteristics of low memory consumption, easy expansion, simple concept, and easy implementation [7].

② Line feature extraction

For the boundary line at the intersection of the patches, the neighboring relationship between the patches is judged according to the spatial position relationship of the boundary points. The closest distance between the boundary points of the patch is less than the preset threshold is judged as adjacent, and the one greater than the preset threshold is not related. Neighbor, for adjacent patches, use the patch parameters to calculate the patch line equation. In order to express the spatial range of the intersection line, the boundary points whose distance to the intersection line is within the threshold range are projected to the intersection equation to obtain the coordinates of the projection points, and the effective range of the projection points is taken as the intersection line segment.

③ Registration primitives and similarity measures

Automatic registration of point cloud data based on geometric features is mostly based on rotation invariants (for example: spin image, curvature, etc.). Rotational invariants of line features include: line length, angle between line and line, vertical distance, etc. Due to the characteristics of terrestrial laser 3D scanning (resolution, occlusion), we cannot guarantee perfect consistency between lines with the same name. In addition, unlike two-dimensional space, a pair of lines with the same name in a three-dimensional space cannot establish a conversion relationship between two point cloud data sets, and at least two pairs of non-parallel space lines are required. Therefore, we propose to use two non-parallel spatial straight lines (line pairs) as the registration primitives, and use their three-dimensional spatial rotation-invariant characteristics of the included angle and vertical distance as the similarity measure in the automatic registration of this research. The candidate line pair with the same name is determined in the quasi-two stations.

④ Matching strategy

Matching process: take the line pair feature as the registration primitive, take the included angle and the vertical distance as the similarity measure, iteratively complete the automatic

matching between two adjacent stations, and use the midpoint of the perpendicular line of the line pair with the same name as the point with the same name to calculate the transformation relationship.

1.2 Bridge surface reconstruction based on three-dimensional Delaunay triangulation

1.2.1 3D Delaunay triangulation

3D Delaunay triangulation is also called tetrahedron, because the input three-dimensional point set is also a kind of mapping of three-dimensional space entities, and the basic simplex of the volume is a tetrahedron, and any volume can be divided into multiple tetrahedrons to express, so the result of the 3D Delaunay triangulation of the sample point set is actually a set of tetrahedrons, and what the algorithm needs is the triangles of these tetrahedrons [8]. Tetrahedron triangulation plays an important role in 3D modeling, but tetrahedral triangulation is a very heavy and time-consuming task, but the related algorithms and their applications are quite mature, for example, CGAL (The Computational Geometry Algorithms Library)) 3D Triangulation Data Structure module and TetGen triangulation. Considering the operability of the model and the convenience of data usage, we decided to use TetGen here.

1.2.2 Bridge surface reconstruction

The algorithm is essentially a greedy algorithm applied to surface reconstruction, that is, new triangles need to be selected based on the built surface, this requires a starting condition to start the algorithm and complete the initialization, and then select the triangular patches to add according to the specific topological constraints and triangle selection criteria, and finally the reconstructed surface is generated.

1.3 Detection of potential damage area of bridge

Using a three-dimensional laser scanner to detect potential damage to small and medium-span bridges, based on the advantages of point clouds that can generate a three-dimensional model, establish a digital surface model (DSM) of the lower surface of the bridge, and generate chromatograms to analyze and compare the deformation of the left and right bridges. Use this to determine the potential deformation area. The transverse and longitudinal profile lines along the centerline of each bridge in the DSM of the bridge surface are extracted, the largest deformation areas in the left and right auxiliary bridge spans are analyzed, and the GB-SAR time series displacement method is combined to obtain the potential damage area of the bridge.

2 GB-SAR precise flaw detection in small and medium-span bridge areas

2.1 Essen-Froome atmospheric parameter optimization and correction model considering bridge characteristics and microwave transmission distance

The traditional method of atmospheric parameter correction is to directly establish the mathematical relationship between atmospheric refractive index and displacement to calculate the atmospheric parameter correction value, without considering the layout of the GB-SAR instrument and the geometric characteristics of bridge structure. Dynamic deflection of bridge refers to the deformation value in the projection direction when the bridge is bent, while GB-SAR directly measures the radial displacement of the bridge, which needs projection calculation. In this paper, the instrument layout and the mathematical relationship between the geometric characteristics of bridge structure and atmospheric refractive index in GB-SAR dynamic deflection monitoring of small and medium-span bridges are experimentally studied,

and the atmospheric parameters optimization correction projection model of GB-SAR small and medium-span bridge monitoring based on bridge characteristics and microwave transmission distance is constructed.

When the GB-SAR radar wave propagates in the atmosphere, the intensity of the radar wave signal will attenuate with the extension of the propagation distance. The longer the distance, the stronger the attenuation effect, and vice versa. The intensity of the radar wave signal directly affects the accuracy of the monitoring data. Therefore, this research uses experimental methods to determine the atmospheric parameter optimization correction projection model that takes into account the microwave transmission distance correction number $f(h)$, as follows:

$$d_v = (h - \sqrt{\frac{d_r^2 2h}{n_i^2 \sin^2 \alpha} + h^2}) - f(h) \quad (1)$$

Where d_v is the displacement, d_r is the radial displacement, h is the height from the radar base point to the lower surface of the bridge body, n_i is the atmospheric refractive index

2.2 W-ESMD two-stage noise reduction method

The steps to construct a W-ESMD two-stage noise reduction model based on multi-wavelet threshold and ESMD are as follows [10,11] :

①First-level noise reduction model for bridge dynamic deflection signals. The optimal ESMD modal decomposition method is used to decompose the bridge dynamic deflection signal into a series of sub-signals and an adaptive global average, and the high frequency and low-frequency IMF are distinguished by the mutual information entropy method. For the decomposed high-frequency IMF, the heursure rule, hard threshold and high decomposition scale are used for noise reduction, and for the decomposed low-frequency sub-signal, the heursure rule, hard threshold and low decomposition scale are used for noise reduction. Reconstruct the noise-reduced IMF and adaptive global moving average to obtain the first-level noise-reduced signal.

②Secondary noise reduction model for bridge dynamic deflection signals. Most of the high-frequency noise of the bridge's dynamic deflection signal processed by the first-level noise reduction model has been eliminated. However, the high-frequency IMF decomposed by ESMD still has a lot of low-frequency noise information unprocessed. In addition, considering the influence of the modal aliasing effect in the ESMD modal decomposition process, the signal after the first-level noise reduction still has a small amount of high-frequency noise information and more low-frequency noise information. Therefore, it is necessary to construct a secondary noise reduction model to further eliminate the influence of noise information. The optimal ESMD modal decomposition method is used to decompose the first-level denoised signal into a series of sub-signals and an adaptive global moving average. High frequency and low-frequency IMF are distinguished by mutual information entropy method, for decomposed high-frequency IMF, use heursure rule, hard threshold and low decomposition scale for noise reduction; for decomposed low-frequency IMF, use min-max rule, soft threshold and moderate, and the modal decomposition scale for noise reduction. Reconstruct the noise-reduced IMF and the adaptive global average to obtain the signal after the second-level noise reduction. Realize the noise reduction processing of ground-based microwave interferometric measurement of bridge dynamic deflection signals.

2.3 Damage identification of small and medium-span bridges based on instantaneous frequency and instantaneous energy

- (1) Using the ESMD optimal modal decomposition method, the small and medium-span bridge dynamic deflection after atmospheric parameter correction and two-stage noise reduction processing is decomposed into a series of sub-signals and an adaptive global average.
- (2) Establish the quasi-extremum point extraction criteria of the ESMD optimal modal decomposition sub-signal, use direct interpolation to analyze the frequency spectrum of each sub-signal, establish a calculation model for the instantaneous frequency drop of small and medium-span bridges, and construct the instantaneous frequency distribution Figure, accurately identify whether there is damage to the small and medium-span bridge.
- (3) Construct the mathematical relationship between the frequency ratio of sub-signal decomposed by ESMD in different monitoring periods and the structural stiffness loss, correct the Nishimura damage judgment criterion, and establish the safety level index of the health status of small and medium-span bridges.
- (4) Combining the factors that affect bridge deformation during the dynamic loading process of small and medium-span bridges and the instantaneous frequency distribution diagram of each, analyze the physical meaning of each IMF, and perform statistical analysis on nonlinear IMF to extract damage spikes to accurately identify small and medium spans The time and location of the bridge damage.

3 PSP-InSAR damage analysis of small and medium span bridges

① Select PS point pair

The core step of the PSP-InSAR algorithm is to iteratively build the PSP grid and estimate the relative deformation rate and relative elevation difference between PS pairs. Since the two PS points forming a PS pair are relatively close, the atmospheric phase term $\Delta\varphi_{atmo}$ and the orbital error phase term $\Delta\varphi_{track}$ in the interference phase are basically the same, then the interference phase difference of the two PS points can be modeled as:

$$\delta\phi_{a,i} = \frac{4\pi}{\lambda} \left(T_i \delta v_a + \frac{B_i \delta h_a}{r \sin \theta} \right) + \varepsilon_{a,i} \quad (2)$$

Where, T_i represents the time of the i SAR image relative to the reference SAR image, δv_a represents the relative deformation rate of the two PS points in the a PS pair, and B_i represents the effective baseline of the i interferogram, δh_a represents the relative elevation difference of the two PS points in the a PS pair, r represents the slope distance of the target point, θ represents the lower viewing angle, and $\varepsilon_{a,i}$ represents noise and unmodeled errors. Generally speaking, if $\varepsilon_{a,i}$ is small, then this pixel pair can be considered as a PS pair, and is called PSP.

In order to judge PSP from the mathematical model, you can first define the time correlation coefficient of the a PSP:

$$\gamma_a = \max_{\delta v_a, \delta h_a} \left| \sum_i \omega_{a,i} \exp(j\varepsilon_{a,i}) \right| = \max_{\delta v_a, \delta h_a} \left| \sum_i \omega_{a,i} \exp \left(j \left(\delta\phi_{a,i} - \frac{4\pi}{\lambda} \left(T_i \delta v_a + \frac{B_i \delta h_a}{r \sin \theta} \right) \right) \right) \right| \quad (3)$$

Where $\omega_{a,i}$ represents the weight value corresponding to the a pixel in the i interference image. In simple cases, it can all be set to 1. During the processing, the unknown parameters δv_a and

δh_a Best estimate, then calculate γ_a . At the same time, set the time correlation coefficient threshold $\gamma_{Threshold}$, when $\gamma_a > \gamma_{Threshold}$, this pixel pair can be judged as a PS pair.

② Establish a PSP grid and select a set of PS points

Through the PS pair decision theory described in equation (3), the first PS point is connected to the n th PS point, and finally select a set of PS points in the entire image, and establish a grid.

③ Estimate the relative deformation rate and relative elevation difference between PS pairs

Compared with the traditional PS-InSAR algorithm, the PSP-InSAR algorithm has greatly improved both the PS point density and the PS deformation measurement accuracy, which can provide technical support for the practical application of InSAR technology.

4 Conclusions

Based on the accurate assessment of the safety performance of small and medium-span bridges, this paper proposes a key technology for multi-mode remote sensing collaborative monitoring and precise flaw detection of small and medium-span bridges integrating TLS, GB-SAR and PSP-InSAR. This research has been successfully applied to more than 10 typical bridges, including small and medium-span urban bridges, railway bridges and ancient bridges, and successfully analyzed the safe operation status of bridges to ensure the healthy operation of bridges. For example, Zhaozhou Bridge, an ancient bridge with a long history, has successfully detected the key location of its abnormality, effectively ensuring the safety and stability of the ancient bridge, extending the service life of cultural relics protection, and the direct benefits of the monitoring and evaluation of the ancient bridge. The indirect benefit is more than 60 million yuan. Application results show that this project can effectively improve the level of refinement and intelligence of bridge safety detection, enhance people's recognition of the safety of small and medium-span bridges, and create significant economic and social benefits.

REFERENCES

- [1] Lee J, Shinozuka M. A vision-based system for remote sensing of bridge displacement. NDT & E International, 2006, 39(5): 425-431.
- [2] Anita S, Stuart R, Barry G. Structural monitoring for the rail industry using conventional survey, laser scanning and photogrammetry. Applied Geomatics, 2015, 7(2): 1-16.
- [3] Pieraccini M, Fratini M, Parrini F, Atzeni C. Dynamic Monitoring of Bridges Using a High-Speed Coherent Radar. IEEE Transactions on Geoscience and Remote Sensing, 2006, 44(11): 3284-3288.
- [4] Stabile T A, Perrone A, Gallipoli M R, Ditommaso R, Ponzio F C. Dynamic Survey of the Musmeci Bridge by Joint Application of Ground-Based Microwave Radar Interferometry and Ambient Noise Standard Spectral Ratio Techniques. IEEE Geoscience and Remote Sensing Letters, 2013, 10(4): 870-874.

- [5] Ferretti A, Prati C, Rocca F. Nonlinear subsidence rate estimation using permanent scatterers in differential SAR interferometry. *IEEE Transactions on Geoscience and Remote Sensing*, 2000, 38 (5) :2202-2212.
- [6] Costantini M, Falco S, Malvarosa F, et al. A New Method for Identification and Analysis of Persistent Scatterers in Series of SAR Images.// *IEEE International Geoscience & Remote Sensing Symposium*. IEEE, 2009.
- [7] Schnabel R, Wahl R, Klein R. Efficient RANSAC for Point-Cloud Shape Detection. *Computer Graphics Forum*, 2007, 26(2):214-226.
- [8] Marc V, Núria P. Computing directional constrained Delaunay triangulations. *Computers & Graphics*, 2000, 24(2):181-190.
- [9] Essen L. and Froome K D. The Refractive Indices and Dielectric Constants of Air and its Principal Constituents and 24,000 Mc/s. *The Proceedings of the Physical Society*, 1951, 64(10): 863–875.
- [10] Wang J L, Li Z J. Extreme-Point Symmetric Mode Decomposition Method for Data Analysis. *Advances in Adaptive Data Analysis*, 2013, 05(3): 1137-1137.
- [11] Liu X L, Li S N, Tong X H. Two-Level W-ESMD Denoising for Dynamic Deflection Measurement of Railway Bridges by Microwave Interferometry. *Selected Topics in Applied Earth Observations and Remote Sensing, IEEE Journal of*, 2018, 11(12):4874-4883.

Sessions

Producing DEM using Drone 3D Point Cloud

JaeHo Won* • Mihwa Song** • Min Heo*** • Suk-Bae Lee****

ABSTRACT: Currently, 3D point cloud data acquired using drones is mostly used in the production of digital surface models(DSM). In this study, a digital elevation model (DEM) was constructed using three-dimensional point cloud data. For this, 3D point cloud data extraction, automatic classification, and DEM generation were performed. As a result, this paper presents the possibility of producing a drone-based DEM.

Keywords: UAV¹; 3D Point Cloud; DEM;

1.Introduction

This study suggests the possibility of producing DEM using drone that can quickly photograph small areas. DEM producing process using drone is shown in Figure 1.

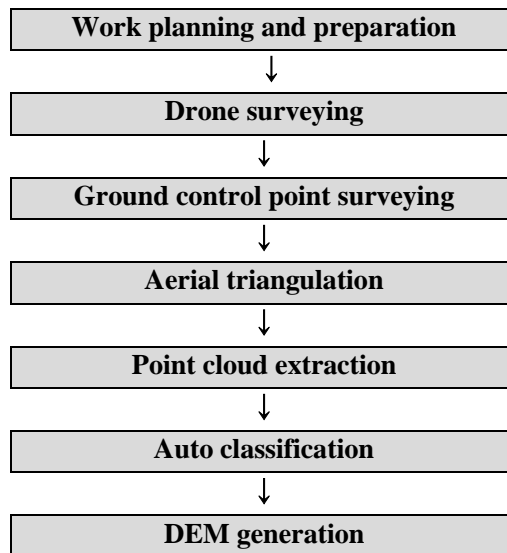


Figure 1. DEM producing process

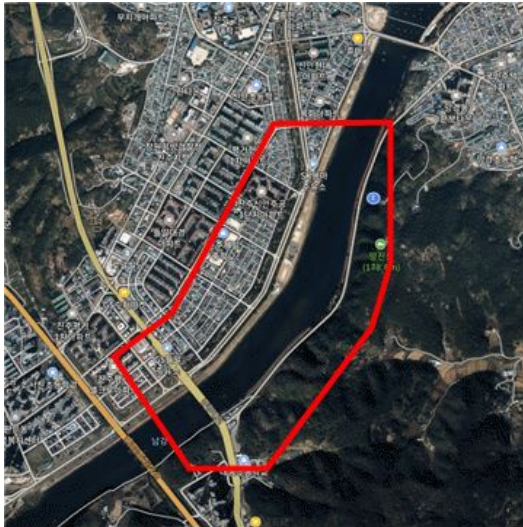
* Corresponding author, Research professor, WonKwang University, aerowon@nate.com

** Senior Researcher, Korea Expressway Corporation Research Institute, mihwa@ex.co.kr

*** Director, UOK Ltd., heomin61@gmail.com

**** Professor, Gyeongnam National University of Science and Technology, sblee@gnitech.ac.kr

The pilot site is the Namgang-river area in Jinju-Si, which includes various terrains. The area includes buildings, roads, rivers and mountains and covers an area of 1.4 km².



(a)



(b)

Figure 2. (a)The pilot site(Namgang-river area) (b) Ground control points

The drone used in this study is the DJI Inspire-2 and the camera is the DJI X5. There is 15 ground control points and Pix4DMapper is used for dense point cloud extraction. The point density of the point cloud is 34 pts/m².



Figure 3. Dense point cloud

2. Experimental Section

In this study, the automatic classification was performed with six kinds of software(Pix4DMapper, GlobalMapper, Inpho, Trimble Business Center, Metashape, Terrascan), and the DEM was produced using the automatically classified ground data.

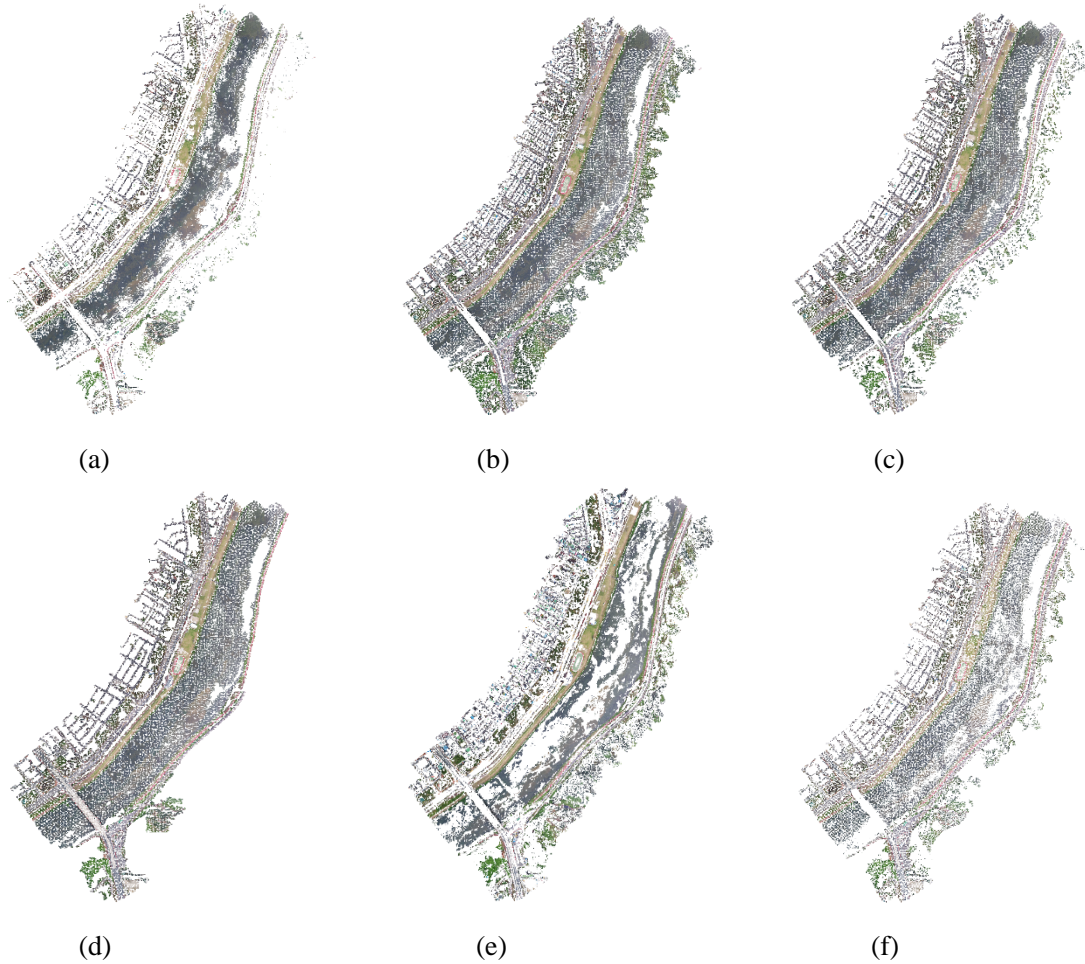
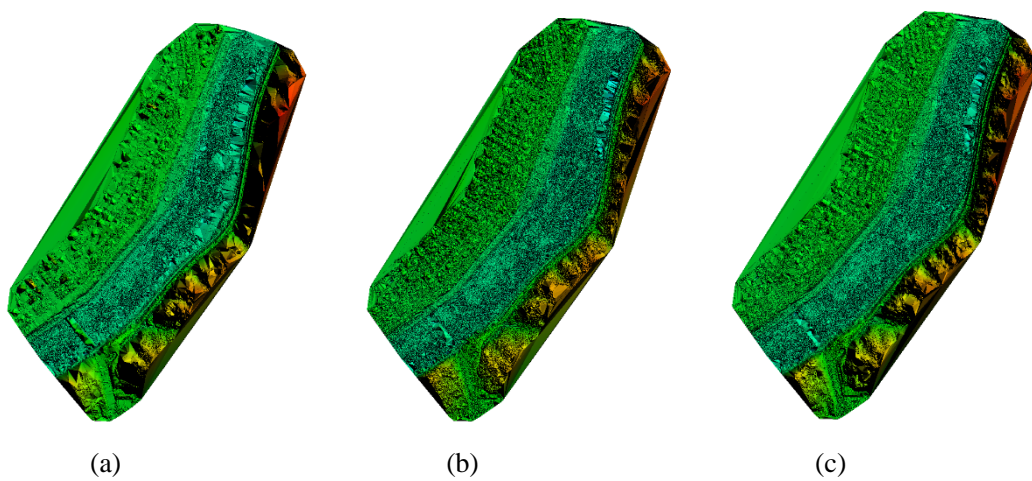


Figure 4. Ground data (a)Pix4DMapper (b)GlobalMapper (c)Inpho (d)Trimble Business Center (e) Metashape (f)Terrascan



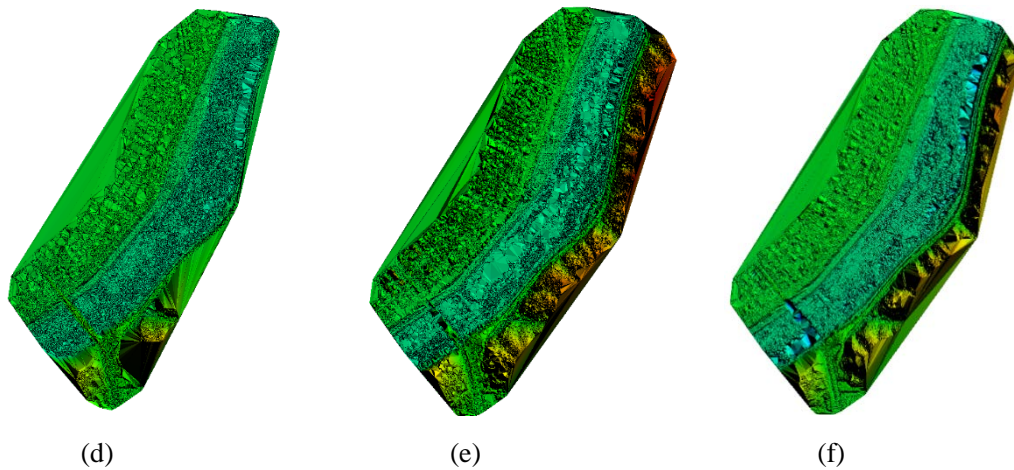


Figure 4. DEM (a)Pix4DMapper (b)GlobalMapper (c)Inpho (d)Trimble Business Center (e) Metashape (f)Terrascan

3. Results and Discussion

The mountainous area were so dense that it was impossible to produce a DEM in all software. In Trimble Business Center, bridge existed in the ground data and Terrascan had the best overall automatic classification performance.

4. Conclusion

In order to produce a good DEM, Manual classification is necessary because automatic classification is not perfect in all software. And in order to produce DEM in dense mountain area, complementary survey using Lidar is required. This study confirmed that producing DEM using drone is possible.

Acknowledgement

This work was supported by the Korea Expressway Corporation as a 2019 research project.

References

- 1) Kim, D.I., Song, Y.S., Kim, K.H., and Kim, C.W., 2014, A study on the application of UAV for Korean land monitoring, Journal of the Korean Society for Geospatial Information Science, 32.1, 29-38.
- 2) Lee, B.G., 2018, A Study of Three Dimensional DSM Development using Self-Developed Drone, J. Korean Earth Sci. Soc., 39.1, 46-52.
- 3) Tran, D.X., Pla, F., Carmona, P.L., Myint, S.W., Caetano, M., and Kieu, H.V., 2017, haracterizing the relationship between land use land cover change and surface temperature, ISPRS Journal of Photogrammetry and Remote Sensing, 124, 119-132.
- 4) Kim, J. and Kim, E.J., 2019, Application of Eco-friendly Planning of Sinseo Innovation City in Daegu using the Analysis of Satellite Image and Field Survey, Journal of the Korean Society of Surveying, Geodesy, Photogrammetry and Cartography, 37.3, 143-156.

Deformation Monitoring in Expressway Infrastructure Construction Using Drone

Suk-Bae Lee^{*2} • Mihwa Song^{**} • Sukgu Kim^{***} • Jae-Ho Won^{****}

ABSTRACT: Today, UAVs (Unmanned Aerial Vehicles) are used not only in the mapping field but also in various field as like forest research, search and rescue, and drone delivery etc. This study examines the possibility of deformation monitoring using UAV at the expressway construction field in Korea. For this study, UAV photogrammetry were performed three times and the ortho-image, DEM and 3D topographic model of the construction field were produced through data processing. In addition, it was checked the construction status of the earthwork and structure work through time series images and overlapping the 3D model with design drawings. In this study, it is concluded that it is possible the deformation monitoring using UAV photogrammetry in expressway infrastructure construction.

Keywords: UAV: 3D topographic model: deformation monitoring: ortho-image: expressway construction field

1.Introduction

This study examines the possibility of deformation monitoring and construction management using UAV at the expressway construction field in Korea. For this study, UAV photogrammetry and ground control point survey were conducted in accordance with the Korean National Geographic Information Institute's 「Guidelines for the Public Survey Using UAV」 at Korea expressway construction field. The ortho-image, DEM and 3D topographic model of the construction field were produced through data processing. And, we tried to check the construction status of the earthwork and structure work through time series images and overlapping the 3D model with design drawings.

2. Experimental Section

This study is intended to monitor the deformation in Expressway Infrastructure Construction using drones. The definition of deformation monitoring is to monitor changes in construction situations, such as earthworks and structural works, and to evaluate whether the construction status is consistent with the design. To this end, the test bed was selected and the UAV photogrammetry was performed. The test bed was selected as the construction field of the Pyeongtaek-Seopyeongtaek expressway, and the UAV photogrammetry was performed three times a month. Table 1 shows an overview of UAV

* Corresponding author, Professor, Gyeongnam National University of Science and Technology, sblee@gntech.ac.kr

** Senior Researcher, Korea Expressway Corporation Research Institute, mihwa@ex.co.kr

*** CEO, Geospatial Information Ltd., gpskorea@hanmail.com

**** Research professor, WonKwang University, aerowon@nate.com

photogrammetry, and Figure 1 shows the flight path and pre-processing results of UAV photogrammetry carried out three times in this study.

Table 1. Overview of UAV photogrammetry adopted in this study

Order	Photographing Date	GSD	Overlap ratio	Shooting Area(km ²)	Flight time (minutes)	Number of image
First	17, Jul. 2019	4cm	Long 80% Side 70%	1.5	57	731
Second	02, Aug. 2019	4cm	Long 80% Side 70%	1.5	65	698
Third	29, Sep. 2019	4cm	Long 70% Side 70%	1.5	60	747



(a) 1st photographing preprossing (17, Jul)



(b) 2nd photographing preprossing (02, Aug)



(c) 3rd photographing preprossing (29, Sep)

Figure 1. Each flight path and preprossing results of three UAV photogrammetry

3. Results and Discussion

Drone photographing was carried out using fixed-wing eBee (Sensefly, Swiss) in the Pyeongtaek-Seopyeongaek expressway construction field, ground control point survey was performed by GNSS network-RTK method for plane and by leveling method for height. The data processing of images obtained by drone was processed using three commercial software - Pix4DMapper, Matashape and ContextCapture - and compared the results. Figure 2 shows the DSM and Ortho-image, the results of the UAV photogrammetry respectively, performed in three UAV photogrammetry. Figure 3 shows deformation monitoring of each work using ortho-image in Pyeongtaek-Seopyeongaek expressway

construction field, which enables the deformation monitoring using UAV photogrammetry in expressway infrastructure construction.

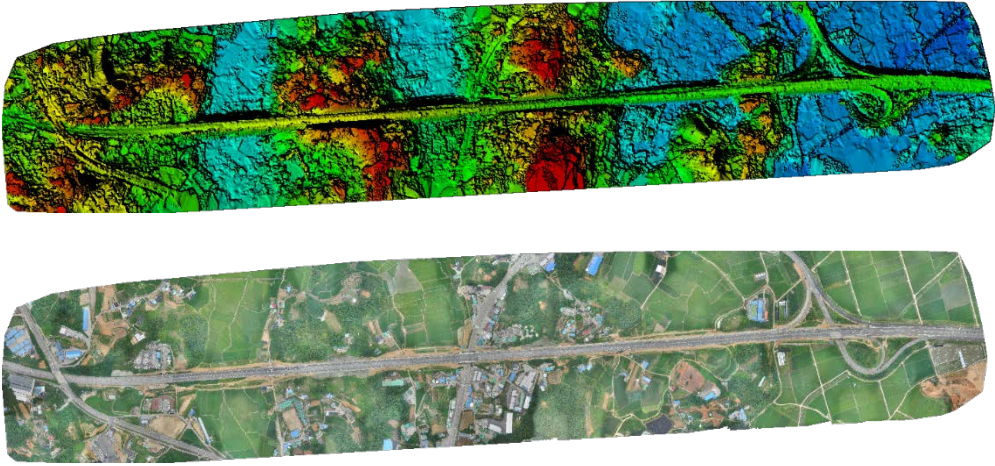
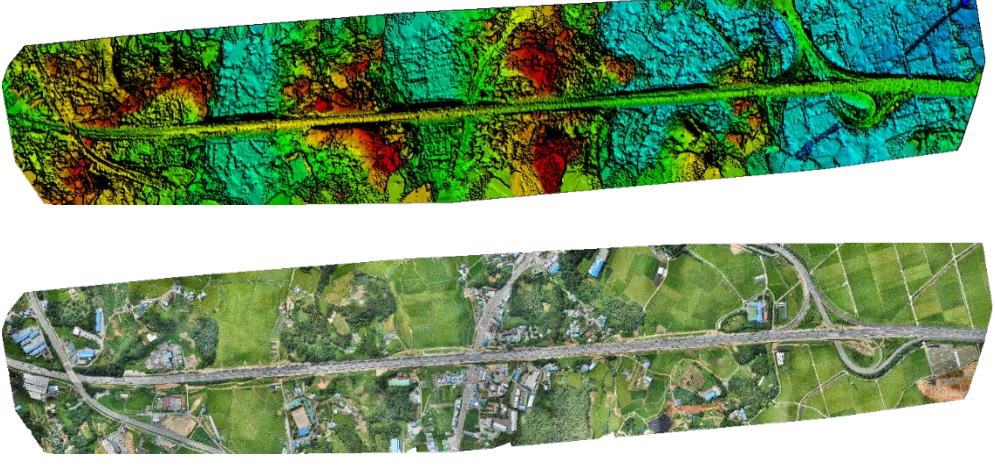
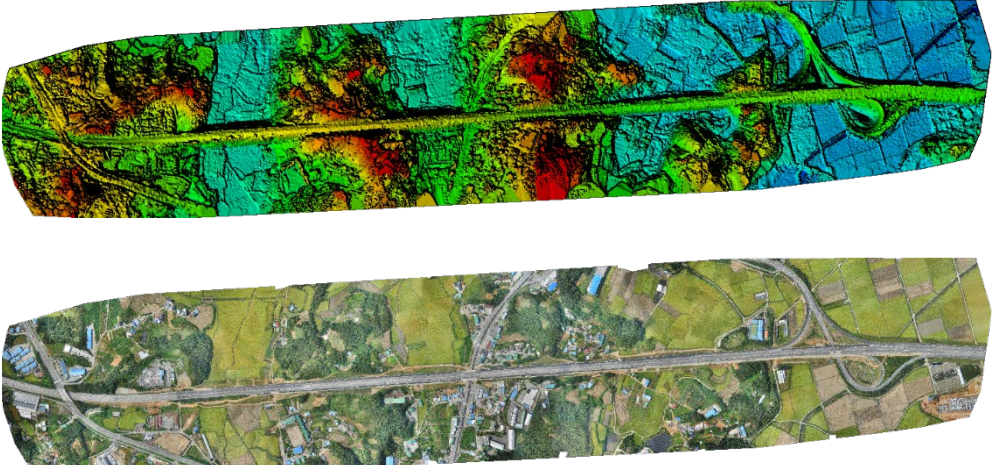
<p>(a)</p> <p>1st Output (17, Jul)</p> <p>DSM and Ortho- image</p>	
<p>(b)</p> <p>2nd Output (02, Aug)</p> <p>DSM and Ortho- image</p>	
<p>(c)</p> <p>3rd Output (29, Sep)</p> <p>DSM and Ortho- image</p>	

Figure 2. Three sets of UAV photogrammetry output (DSM and Ortho-image)



(a) Earthworks

(b) Drainage on slope



(c) Structure works

(d) Side slope construction

Figure 3. Deformation monitoring of each work using ortho-image in Pyeongtaek-Seopyeongtaek expressway construction field

4. Conclusion

In this study, it is concluded that it is possible the deformation monitoring using UAV photogrammetry in expressway infrastructure construction.

Acknowledgement

This work was supported by the Korea Expressway Corporation Research Institute as a 2019 research project.

References

- 1) KECRI, 2019, A Study on the Plan Establishment of Standard Work and Pilot Operation for Use of Drones in Construction Field, Korea Expressway Corporation Research Institute, Report

- 2) Lee S.B., Kim T., Ahn Y.J. and Lee J.O., 2019, Comparison of Digital Maps Created by Stereo Plotting and Vectorization Based on Images Acquired by Unmanned Aerial Vehicle, Sensors and Materials, Vol. 31, No. 11, pp. 3797–3810

Factors related to the “Ikigai” among elderly participating in community-based activities in Nagasaki, Japan

○Nakao Rieko (rieke@nagasaki-u.ac.jp) Nagasaki University
 Nitta Akiko (n.akiko.an@outlook.jp) Nagasaki Wesleyan University
 Ohnishi Mayumi (mohnishi@nagasaki-u.ac.jp) Nagasaki University

ABSTRACT: The present study aim is to investigate the factors related to “ikigai” (“ikigai” means purpose in life) among elderly in community residents. A self-administered questionnaire was carried out to the elderly residents who were participated in two community activities in hillside residential area, Nagasaki city. Total 32 elderly residents (Male7, Female 25, mean age $74.3 \pm SD4.9$) were respondent. As the results, "ikigai" score was not related to sociodemographic factors, but related to self-rated health and mental health (GDS-15) ($p = 0.001$, $p = 0.020$, respectively). Statistically significant correlation between “ikigai” and social participation, health status, and mental health were showed ($p=0.017$, 0.007 , 0.007 , respectively). Increasing social participation may increase "ikigai", and prevent frailty and depression in the elderly. Maintaining the elderly's social participation in the community will be effective for health promotion of elderly.

1. INTRODUCTION

Japanese people are noted for the longevity, that life expectancy (81.1 years old for male, 87.1 years old for female) is reported the longest in the world (WHO, 2018). Physical and mental good health contributed to that longevity; additionally some papers were reported that longevity was related to "ikigai". “Ikigai” is a Japanese word which is meaning for purpose in life, that is defined as something to live for, the joy and goal of living. High “ikigai” was reported to reduce all-cause mortality or cardiovascular diseases incidence, and improved well-being or happiness. Therefore, we conducted a study on “ikigai” for elderlies who were participating in community activities. The aim of this study is to make clear the factors related to the “ikigai” among elderly who are participant in community activities.

2. METHODS

1) Study subjects and methods

A self-administered questionnaire was carried out to elderly residents who were participants of two community activities at typical of hillside city area in Nagasaki City. The questionnaire included on socio-demographics (age, sex, family structure, education and self-rated economics status), social participation, self-rated health, mental health status (Geriatric Depression Scale-15, GDS-15) and “ikigai” score. “Ikigai” score was evaluated by using visual analog scale. Visual analog scale is a method of marking the strength of one's point on a 10 cm line and showing a score. GDS-15 is the mental health indicator that the depression tendency becomes worse as the total score increases. GDS-15 score range is from 0 to 15, with 4 or less is normal and 5 or more is depression tendency. Self-rated health was scored 0 point for very good/good or 1 point for fair/poor. Social participation were answered in a multiple choice question from participation of nine items, such as community events, residents' associations, seniors' clubs, hobby clubs, volunteer activities, teaching activities, childcare support activities, elderly support activities and support for community center activities. And, the description in the comment section of the questionnaire was qualitatively assessed.

The questionnaire was conducted at the time of community activities, and the responses were collected anonymously. The investigation period was from August to September, 2018.

This study was approved by the Ethical Committees of Nagasaki University Graduate School of Biomedical Sciences (authorization No. 18080909).

2) Statistical analysis

Mean scores of "Ikigai" were compared by socio-demographic characteristics and health status (self-rated health and mental health) using unpaired t-test or one-way ANOVA. Spearman's rho correlation was used to determine the association between "ikigai" score and the total number of social participations or health status (GDS-15, Self-rated health). The statistical significance was set at $p < 0.05$. IBM SPSS statistics version 20 was used for statistical analysis.

3. RESULTS

A total of 32 elderly residents (7 males, 25 females, mean age $74.25 \pm$ standard deviation; SD4.9, range 66-84 years old) responded to the questionnaire. Table1 showed the socio-demographic characteristics and "ikigai" score of these respondents. In the socio-demographic characteristics, only "sex" showed a statistically significant association with the "ikigai" score. And, table2 showed the comparison of mean score by each health status. Both self-rated health and GDS-15 had a statistically significant association with the "ikigai" score ($p = 0.001$, $p = 0.020$, respectively).

The mean of social participation was 4.13 (standard deviation; SD2.3, range 0-8). Table3 showed that the association between "ikigai" and social participation or each health status. Statistically significant correlation was showed social participation (Spearman's correlation coefficient; $\rho = 0.426$, $p = 0.017$), GDS-15 ($\rho = -0.523$, $p = 0.007$), and self-rated health ($\rho = -0.485$, $p = 0.007$).

Table 4 showed the main descriptions of the participants. A lot of comments were mentioned that participation in community activities was pleasures. We assessed that community activities have be useful improve the quality of life (QOL) for the elderly.

Table1. "Ikigai" score by the socio-demographic characteristics of respondents (N=32)

		n (%)	Ikigai score*	p-value [#]
Sex	Male	7 (21.9)	8.79 \pm 1.3	0.001
	Female	25 (78.1)	6.33 \pm 1.7	
Age category	60-69 years	7 (21.9)	6.43 \pm 2.1	0.201
	70-79 years	22 (68.8)	7.26 \pm 1.8	
	80 years or over	3 (9.4)	5.33 \pm 0.6	
Family structure	Living alone	13 (40.6)	6.39 \pm 1.8	0.471
	Living with spouse	10 (31.3)	7.25 \pm 1.9	
	Living with other members	8 (25.0)	7.25 \pm 1.9	
Educational background	Junior high school	3 (9.4)	7.00 \pm 2.0	0.910
	High school	20 (62.5)	6.78 \pm 1.9	
	University/vocational school	7 (21.9)	7.14 \pm 2.1	
Self-rated economic conditions	Sufficient /comfortable	13 (40.6)	7.42 \pm 2.1	0.238
	Insufficient/ poor	17 (53.1)	6.59 \pm 1.7	
Role in community activities	Volunteers	15 (46.9)	7.68 \pm 1.6	0.032
	Participants	17 (53.1)	6.24 \pm 1.9	

*mean \pm standard deviation (SD), [#] Unpaired t-test or one-way ANOVA were performed.

Table2. “Ikigai” score by self-rated health and the mental health status (N=32)

		n (%)	Ikigai score*	p-value [#]
Self-rated health	Very good/Good	20 (62.5)	7.73±1.8	0.001
	Fair/Poor	10 (31.3)	5.40±0.8	
GDS-15	Normal	18 (75.0)	7.47±1.8	0.020
	Depression tendency	6 (25.0)	5.40±0.9	

*mean ± standard deviation (SD), [#] Unpaired t-test was performed.

Table3. Spearman's correlation between “ikigai” score and health status

	Ikigai	Social participation	GDS-15	Self-rated health
Ikigai	-	0.426*	-0.523**	-0.485**
Social participation		-	-0.357	-0.419*
GDS-15			-	0.278
Self-rated health				-

Spearman's correlation analysis was performed.

** Correlation is significant p<0.01, * Correlation is significant p<0.05

Table4. Description of participants' comments (main items)

Sex (age)	Details
Female (77)	I have few opportunities to go out, so I look forward to participation in this class.
Female (69)	I am participating happily every time. Thank you in the future.
Female (76)	I want to help each other and get along in neighborhood.
Female (76)	I want to spend every day laughingly.

4. DISCUSSION AND CONCLUSION

The "ikigai" score was not related to sociodemographic factors such as family structure, education level, or economic factors, but related to social participations, health status and mental health status. This result may suggest that in any socio-economic situation, maintaining good physical and mental health status may improve “ikigai”. Because the social participations and "ikigai" were correlated with statistically significant, increasing opportunities for social participation may improve "ikigai" of the elderly. In other words, increasing social participation may increase "ikigai", and prevent frailty and depression in the elderly. Promoting the elderly's social participation is important in public health policy of ageing Japanese society. Community activities that the close relationships of residents are created would be more effective.

In addition, community activities were a pleasure for the elderly participants. Community activities had helped improve the quality of life for the elderly.

The limitations of this study were the small number of participants and selection bias toward to healthy elderly people participating in community activities. It is necessary to increase the study participants and conduct further research. Another limitation was that it is a correlation analysis, so it could not be mentioned whether people with a high "ikigai" have a lot of social participation or people with a lot of social participation have a high "ikigai".

ACKNOWLEDGEMENT

We would like to express deep thanks to the residents of Sakamoto-machi and Mizunoura-machi for their contributions. The authors declare that they have no conflicts of interest.

REFERENCES

- 1) Yasukawa S, Eguchi E, Ogino K M, Tamakoshi A, Iso H. (2018). “Ikigai”, subjective wellbeing, as a modifier of the parity-cardiovascular mortality association -the Japan Collaborative Cohort Study-, *Circulation Journal*, 82, 1302-1308, doi: 10.1253/circj.CJ-17-1201
- 2) Tanno K, Sakata K, Ohsawa M, Onoda T, Itai K, Yaegashi Y, Tamakoshi A. (2009). Association of ikigai as a positive psychological fadtor with all-cause mortality and cause-specific mortality among middle-age and elderly Japanese people: Findings from the Japan Collaborative Cohort Study, *Journal of Psychosomatic Research*, 67, 67-75, doi: 10.1016/j.jpsychores.2008.10.018
- 3) Tomioka K, Kurumatani N, Hosoi H. (2016). Relationship of having hobbies and a Purpose in Life ith mortality, activities of daily living, and instrumental activities of daily living among community-dwelling elderly adults, *Journal of Epidemiology*, 26(7), 361-370, doi: 10.2188/JE20150153
- 4) Michaela CS, Niklas Z (2019). Life crafting as a way to find purpose and meaning in life, *Frontiers on Psychology*, doi: 10.3389/fpsyg. 2019.02778

Estimation of the Land Deformation Used by Sentinel-1A SAR Data Applied on Dangjin Reclaimed Area, Korea

Eung-Nam Kim * and Byungdug Jun **

Abstract. Dangjin area of South Korea was conducted to analyze the ground displacement using remote sensing techniques with SAR data. In research area, a vertical hole was excavated for the construction of an electric power hole for the electricity supply facility, and then many of civil complaints related to damage and settlement of nearby structures. It was occurred to the ground displacement of the surrounding area due to the drop in the groundwater level in connection with the construction progress. To solve this problem, it is necessary to analyze the impact on the subsidence of the ground and the condition of the structure before and after excavation of the vertical hole. In this research, estimation and ground displacement was analyzed to find out the reasons of ground displacement using microwave radar images named InSAR technology observed from satellites. In order to analyze the ground displacement during the construction process, multi temporal satellite images observed from the past to the present were used.

Keywords: Interferometric, Dangjin, South Korea

1 Introduction

The digging work of electric power hole of the research target was began on October 17, 2017. However, all construction plan was stopped on February 19, 2019 because of the ground displacement.

Table 1 major all events of the research area Dangjin

Date	major events
2017/10/17	start drilling work moving to the vertical direction of the mail hole
2017/12/25	temporary stop the drilling work to the vertical direction
2018/05/18	restarted drilling work moving to the vertical direction
2018/09/28	start drilling work of the reaching hole with vertical direction
2018/10/18	completion of drilling work moving to the vertical direction
2018/11/20	start tunnel construction from the main hole to the destination hole
2019/02/19	stop the tunnel construction work because of the civil complaints
2019/06/03	water level restoration completed for the water level of destination hole
2019/07/02	start restoration work of the groundwater in main hole
	(no comment of restoration completion)

*Professor, Inha Technical College, kimen@inhac.ac.kr

**Professor, Nagasaki University, bdjun@nagasaki-u.ac.jp

In order to confirm the deformation of the ground target area, a total of 10 scenes of microwave satellite images named SAR observed in the target area was processed. All data from 2015 to 2019 when there were many civilian complaints about the ground deformation were chosen. The patterns of subsidence and the size of deformation extent were calculated.

2 Study Area and Used Software

Research area and the size of each SAR image is as follow.

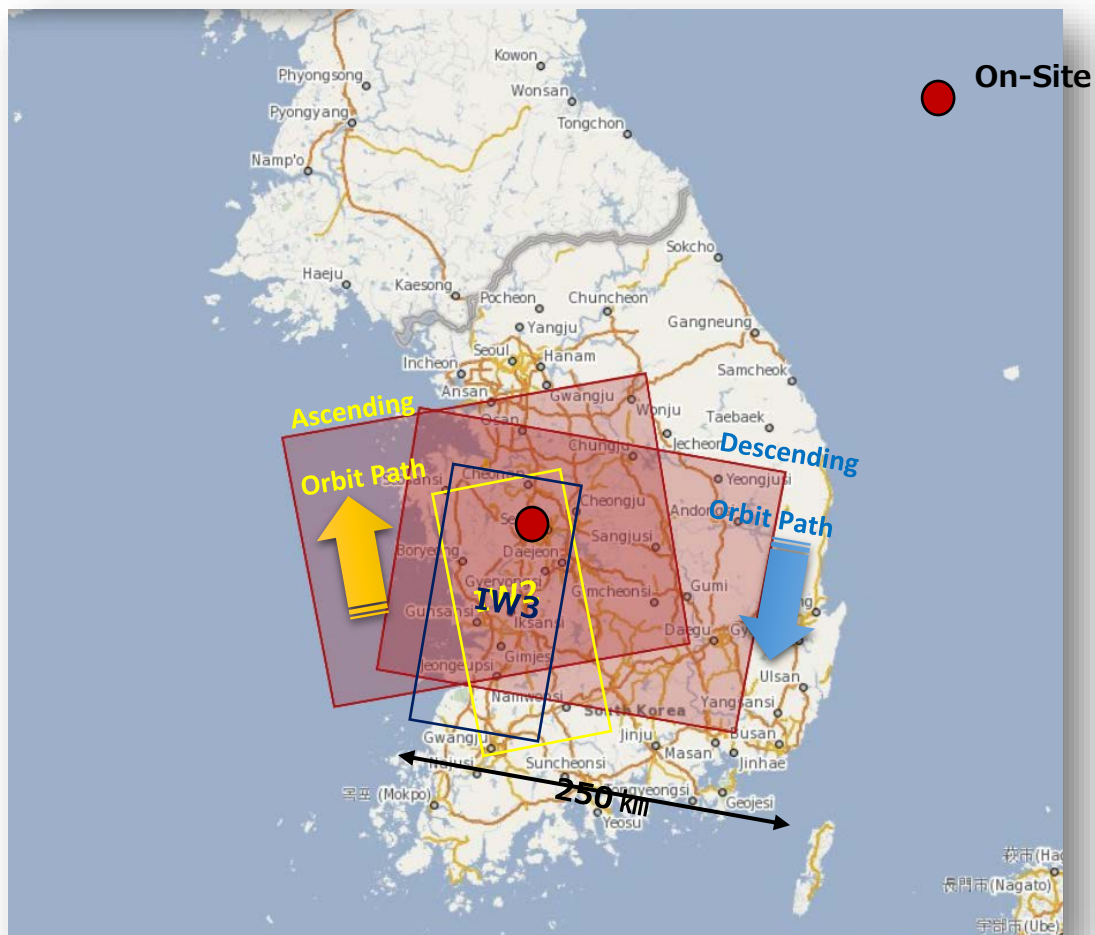


Figure 1 Orbital path of Satellite Sentinel 1A on the research site

From the figure-1 above, the satellite for the image named IW2 is for the ascending orbit path and the satellite image named IW3 is for the descending orbit path. A small red circle is a site for this research area.

To identify the displacement with SAR satellite data, it needs two satellite data the master and slave from the space that observed the spots before and after the natural disaster¹⁾ caused by diastrophism. In this research, the satellite named Sentinel was used. It was employed and loaded with the C-band antenna by the European Space Agency (ESA). The C-band wavelength was 5.6 cm. It means that the

phase difference of the circular term of this band was set to 2.3 cm. The image processing technique, which expresses the repeated numbers as a diastrophism height, is called the phase unwrapping approach for data processing²⁾. A software named SANP (Sentinel Application Platform) was used and applied for deformation analysis.

3 Used Data for ground deformation

Ground deformation analysis utilized satellite images which observed at each corresponding time by surveying the amount of change in the ground deformation between two periods from the first data (March 2016) and the second data (September 2019) conducted before and after the construction in this target area. The relationship between the surveying data and the amount of ground change which was calculated using data (Sentinel-1a) was analyzed. The two satellite (Sentinel-1a) SAR data were based on the image captured on March 1, 2016, and on September 6, 2019. And two data which means Dangjin City data and ERC (Emergency Response Committee) data were used for comparative analysis with comparison between on-site survey data and satellite imagery. Figure 2 is a result of comparison with the survey data of Dangjin City and ERC data. Figure 2 shows no correlation between the survey data of Dangjin City and the ground deformation extracted through image SAR results. On the other hand, it can be seen that the survey data of the ERC showed a certain degree of correlation with the ground deformation amount of Sentinel-1a.

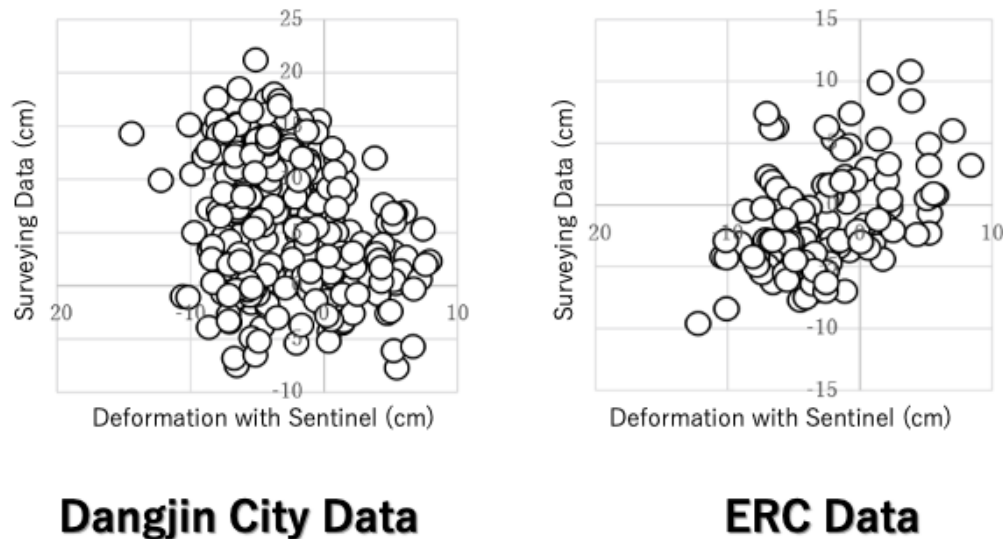


Figure 2 Analyzed results with on-site surveying data and satellite imagery data

Table 2 Sentinel data sets used in this study

Period	main data set	slave data set
first term	2015/11/14	2015/12/20, 2016/1/1
second term	2017/9/16	2017/10/10, 2017/11/3, 2018/1/2
third term	2018/6/19	2018/11/10, 2019/1/21, 2019/2/2, 2019/3/10
whole term	2017/10/10	2019/2/2

Table 2 shows that there are three kinds of term for ground deformation analysis. The first term from December 20, 2015 to January 1st, 2016 is a one period until before tunnel work. First term used the SAR data of sentinel 1A on December 14, 2015 as a main verification data set for interferometric method. Second term from October 10, 2017 to January 2nd, 2018 is another period occurring civilian complaint due to change ground level. Third term from October 10, 2018 to March 10, 2019 is more another period with very changing term of ground area and structure and buildings. Lastly, whole term means including all terms period from October 10, 2017 to February 2nd, 2019. The main data set dated on October 10, 2017. It is basis data for verification with the data on February 2nd, 2019.

4 Results and discussion

Figure 3 shows all analysis results of the amount of ground deformation for each period that occurred ground change in the research target area.

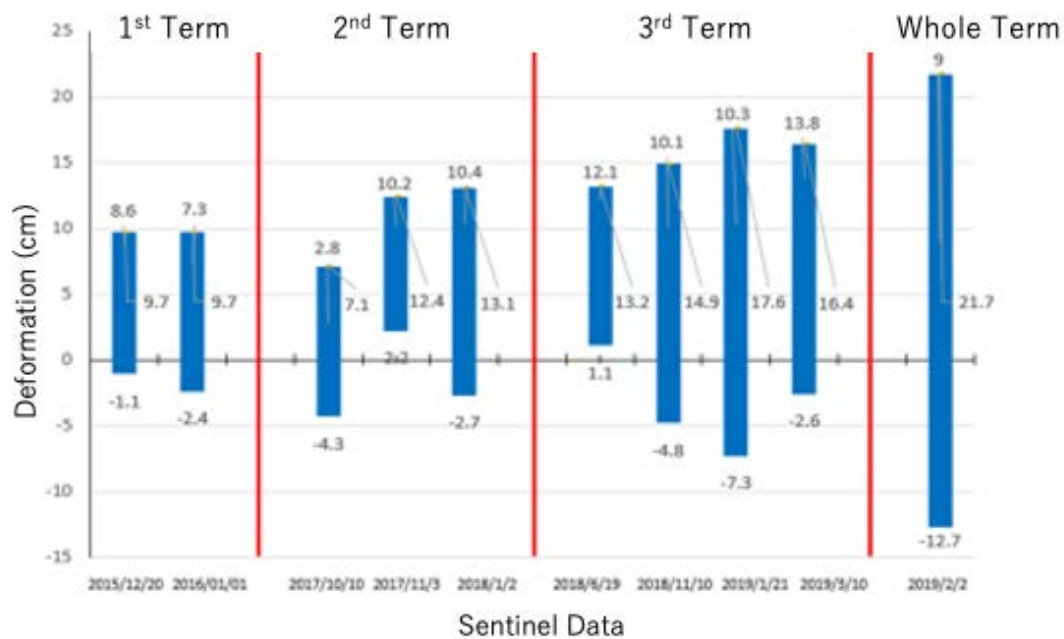


Figure 3 Analyzed results with on-site surveying data and satellite imagery data

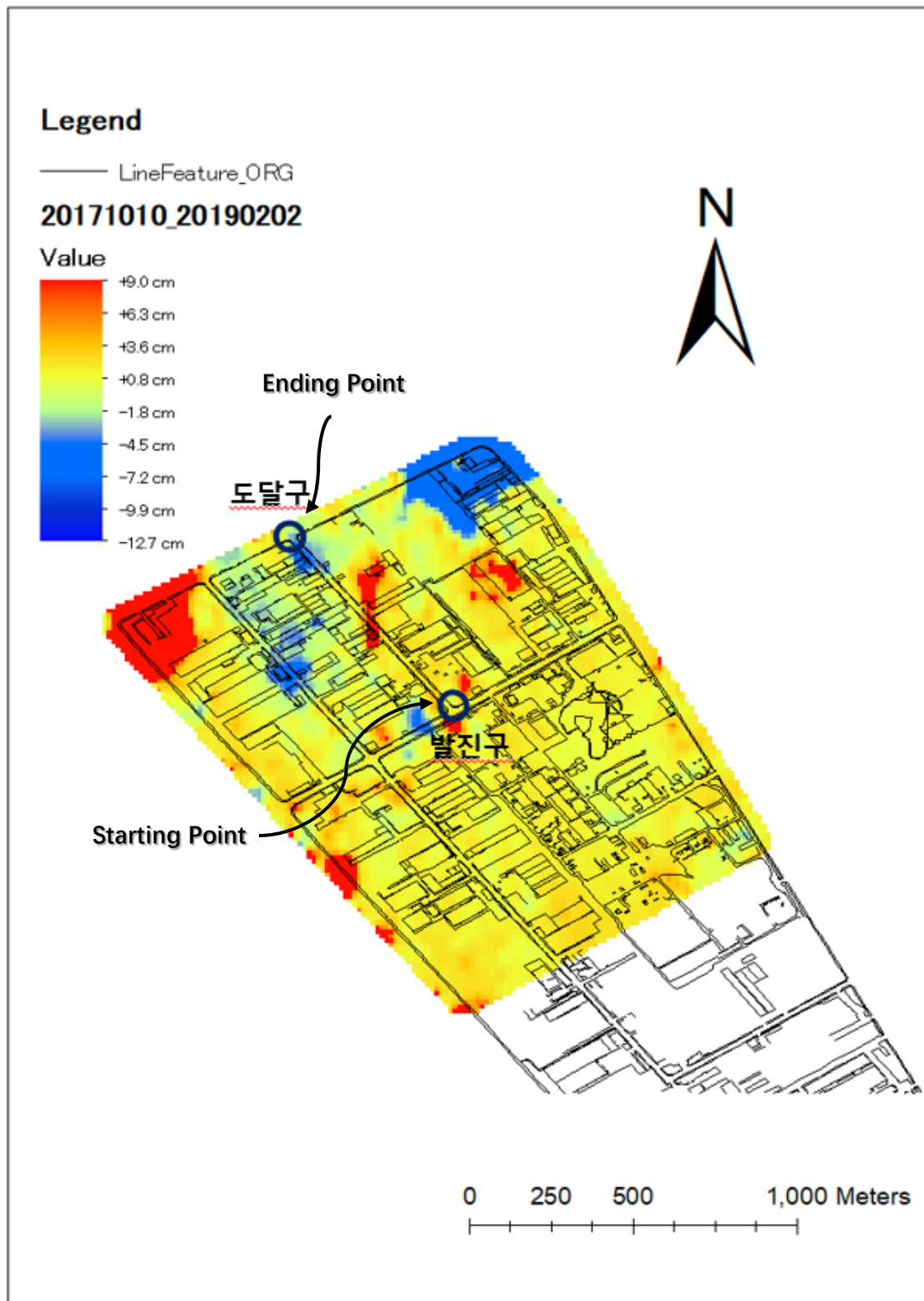


Figure 4 Result of the whole term period for the research target

This result is the amount of ground deformation in the analysis target site corresponds to the range from settlement to top value obtained through image processing (the range of the value shown in the graph of each analysis result). In Figure 3, the period corresponding to the first period corresponds to the period of pure natural subsidence, which took place in the period before to the implementation of the current construction after the reclaiming of the target area was created. In this view, it shows a range of uplift from -1.1cm to 8.6cm of settlement in the first period. At this time, it can be understood that the amount of ground deformation was 9.7cm only. In the second period, a total of 3 images were processed based on the SAR image on September 16, 2016. The first image, October 10, 2017, shows the amount of deformation of 7.1cm, which is similar of the first period, before the start date of the start of the tunnel work. In the images on November 3, 2017 and January 2, 2018, after October 17, 2017, the date of the start of the tunnel work, it can be seen that the amount of ground deformation increased to 12.4 cm and 13.1 cm, respectively.

The third period is the result of processing a total of 4 images based on the images observed on January 2, 2018. During this period, the pumping operation at the starting port, the resumption of excavation of the starting ball immediately, excavation of the reaching vertical holl, and tunnel excavation began. In addition, the time when an emergency civilian complaint was filed due to ground transformation is included. As a result of the analysis, after November 10, 2018, the amount of deformation increased to 17.6 cm and 16.4 cm, and in the image result on January 21, a settlement of -7.3 cm in particular occurred. It can be realized that the width of the amount of ground deformation at the time an emergency civilian complaint was filed was the largest.

In the analysis of the whole term period, as shown in Figure 3 and Figure 4, an emergency civilian complaint was filed based on the image on October 10, 2017, before the start of construction, and the result of processing the image on February 2, 2019, just before the construction was stopped on February 19. to be. As for the settlement, a maximum of -12.7 cm to 9 cm was analyzed, and it was found that the amount of ground deformation reached 21.7 cm.

References

1. Massonnet, D., and K.L. Feigl. 1998. "Radar Interferometry and Its Application to Changes in the Earth's Surface." *Reviews of Geophysics* 36 (4):441–500. <https://doi.org/10.1029/97RG03139>.
2. Zebker, H.A., P.A. Rosen, R.M. Goldstein, A. Gabriel, and C.L. Werner. 1994. "On the Derivation of Coseismic Displacement Fields Using Differential Radar Interferometry: The Landers Earthquake." *Journal of Geophysical Research* 99 (B10):19,617–19,634.

Analysis of Displacement Around Kumamoto Earthquake area Using InSAR Technology

Byungdug Jun* and Eung-Nam Kim**

Abstract. According to an announcement of the Japan Meteorological Agency (2016), the magnitude of a foreshock on April 14 was 6.5 and that of the main shock on April 16 was 7.3. The epicenter was in Mashiki-cho located in the east of Kumamoto City. One of the characteristics of the Kumamoto earthquake was that frequent small-scale aftershocks occurred subsequent to the main quake. If we were to include minor aftershocks that could not even be felt by people, then as many as 130,000 had occurred in the Kyushu region. Even those earthquakes with a magnitude of 3.5 or more have been recorded 339 times. Aftershocks are a common feature of earthquakes and occurred with extraordinary frequency in the case of the Kumamoto earthquake. In this study, displacement of Kumamoto earthquake (magnitude 7.3) was calculated and demonstrated the result of using InSAR technology. we also analyzed and verified the 2016 Kumamoto earthquake data with the SAR data obtained from our investigations. The result of Root Mean Squire Deviation (RMSD) on the verified area was 6.8 with an R^2 of 0.72.

Keywords: Interferometric, earthquake disaster

1 Introduction

Two types of surveillance technologies are used in satellite remote-sensing data. One type of technology recognizes and uses sunlight reflected from the earth's surface, which reaches the image sensors of satellites as information in the visible region of the spectrum. This is a common technology for using satellite images. The other type of technology is InSAR, which generates surface deformation maps using two or more SAR images; variations of an observed location are captured in three dimensions and visualized using the latest computer technology. Increasing attention is now being paid to this technology.

When a sensor tries to survey a point two or more times using the same satellite, InSAR technology can visualize diachronic variations of the location. This makes it possible, for example, to visualize variations in the surface-of-the-earth information of an area where a nuclear test facility is located or to visualize the displacement of an area that is presumed to be a nuclear test site. Until now, this technology has been mainly used for disaster prevention, including observations of the displacements caused by earthquakes (Massonnet and Feigl, 1998)¹. It has also become possible to compute the displacement caused by artificial earthquakes in nuclear tests by applying the same technical concept.

* Professor, Nagasaki University, bdjun@nagasaki-u.ac.jp

**Professor, Inha Technical College, kimen@inhatec.ac.kr

One of the merits of InSAR technology is that it can irradiate using an active wave from the satellite antenna. Therefore, by comparing with the common satellite data using information from sunlight reflection, nighttime observations can be actively made possible. At the same time, we can obtain the movement of the earth's surface for an observation area in case of rainy weather as well. Furthermore, InSAR technology also makes it possible to observe difficult terrains (i.e., mountains, deserts, polar zones, remote areas, and other places that are difficult to navigate). However, this technology also has some weaknesses such as observation errors, orbital errors, ionospheric errors (i.e., atmospheric-air time-delay error), and height errors (Zebker et al., 1994)²⁾. The greatest error to overcome is ionospheric error, that is, the influence of water vapor present between the irradiating radars and sensors that receive the bounced information. When thick water vapor (or the ionized layer) exists between the observed earth and irradiating radars, it is very likely that errors are included in the obtained results (Zebker et al., 1997)³⁾.

2 InSAR technology

To identify the displacement using InSAR technology, we need both the master and slave data from the two SARs that observed the spots before and after the natural or artificial earthquakes caused by diastrophism. In Figure 1, the interference picture images are composed using two data sets in the 2nd step, and the final picture images obtained in the 3rd step are in rainbow colors. As a result, the image shows the actual displacement of the earth's surface as a phase change with rainbow colors visualized by the wavelength changes of the radar. The radar of each satellite scanned the line of sight (LOS) and received the rebounding radar waves. The rainbow-colored variations obtained from the analysis using InSAR technology are repeated like waves (see the 3rd step of Figure 1). The amount of circular terms of the rainbow-colored variation is equal to half the irradiated radar wavelength. The L-band wavelength of the Advanced Land Observing Satellite (ALOS) currently loaded on SAR satellites in Japan is 23.6 cm (Dore et al., 2013)⁴⁾; therefore, the phase difference for the circular term was set to 11.8 cm. The phase difference shows that the variation was approximately 11.8 cm.

The satellite named Sentinel, employed by the European Space Agency (ESA), was loaded with the C-band antenna. The C-band wavelength was 5.6 cm; therefore, the phase difference of the circular term was set to 2.3 cm. If a rainbow-colored phase difference was observed on an overlapping computed image created by InSAR, it meant that there was a displacement of 11.8 and 2.3 cm or more for the L-band and C-band, respectively. When the rainbow-colored phase difference was repeated, we realized that there was a diastrophism or displacement as large as the repeated numbers of the rainbow color. For example, if the rainbow color was repeated twice on a calculated digital image, it can be estimated that a displacement of approximately 11.8 and 2.3 cm had theoretically occurred in the L-band and C-band, respectively. The image processing technique, which expresses the repeated numbers as a diastrophism height, is called the phase unwrapping approach for data processing.

In previous data processing of this study, we chose a natural earthquake that hit the outskirts of Kumamoto, Japan, on April 14, 2017, and verified the displacement using InSAR data. Subsequently, we applied the same method to the area of the artificial earthquake caused by DPRK's sixth nuclear test and showed the potential of satellite surveillance technology using these results.

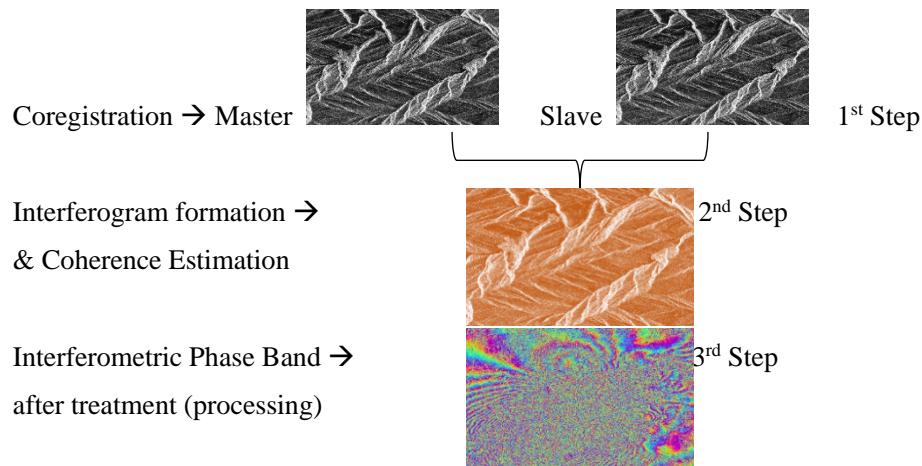


Figure 1: Processing of InSAR technology and the resulting pictures and images

3 Analysis of natural earthquakes using InSAR technology

First, we studied the Kumamoto earthquake (magnitude 7.3) and demonstrated the result of using InSAR technology for analysis. According to an announcement of the Japan Meteorological Agency (2016), the magnitude of a foreshock on April 14 was 6.5 and that of the main shock on April 16 was 7.3. The epicenter was in Mashiki-cho located in the east of Kumamoto City. One of the characteristics of the Kumamoto earthquake was that frequent small-scale aftershocks occurred subsequent to the main quake. If we were to include minor aftershocks that could not even be felt by people, then as many as 130,000 had occurred in the Kyushu region. Even those earthquakes with a magnitude of 3.5 or more have been recorded 339 times. Aftershocks are a common feature of earthquakes and occurred with extraordinary frequency in the case of the Kumamoto earthquake.

This study analyzes seismic activity using the Sentinel Application Platform (SNAP), which was developed under the ESA for the analysis of data obtained using InSAR. We used another software called SNAPHU distributed by SORSEFORGE) to process the phase unwrapping approach data. For the Sentinel satellite SAR data, we downloaded all the data from the Copernicus Services Data Hub, which was run by the ESA, and those data were solely for the SARs named S1A and S1B. The Sentinel satellites carried C-band antennae, which had wavelengths different from the L-band antennae of Japan's SAR satellite ALOS.

In this study, the Sentinel satellite data from the C-band were compared with the ALOS satellite data from the L-band to check the performance of the C-band and L-band. We used data from the analysis of the L-band carried out by the Geographical Survey Institute regarding the Kumamoto earthquake (Geospatial Information Authority of Japan, 2016).

Figure 2 shows the results of the analysis of the L-band obtained from Japan's SAR satellite ALOS and of the C-band from the European satellite Sentinel, both of which cover almost the same area centering on the epicenter of the Kumamoto earthquake. The result shows variations in phase differences expressed as rainbow-colored waves, such as the L-band and C-band. Variations in the phase difference arise from the phase difference between the L-band (having a long wavelength) and the C-band (having a short wavelength) LOS signals. In Figure 2, the circular phase difference of the L-band with a long wavelength is larger than the rainbow-colored phase difference of the C-band with a short wavelength. In Figures 3 and 4, Kumamoto and Tamana with ground control points were chosen as the survey sites; both these sites were close to the epicenter (marked with a red star). Figure 3 shows the phase differences, and Figure 4 shows the displacement as a digital histogram.

(1) Analysis of the Kumamoto earthquake

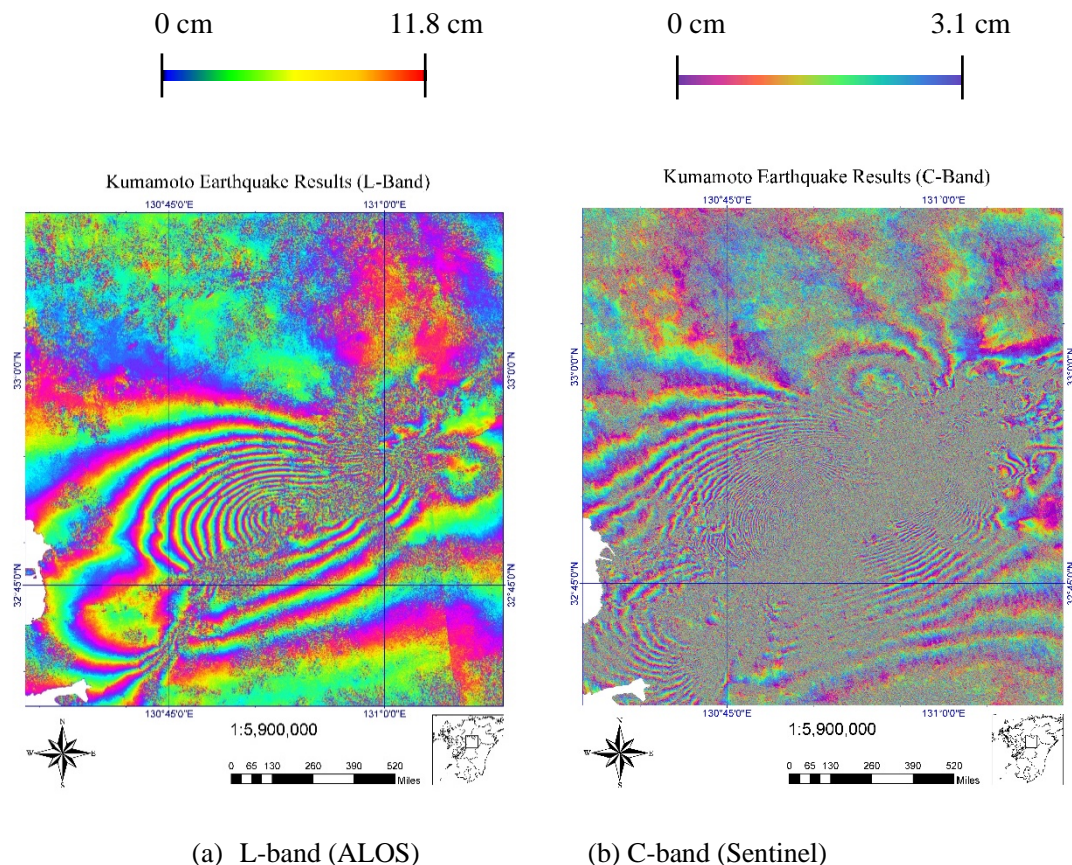
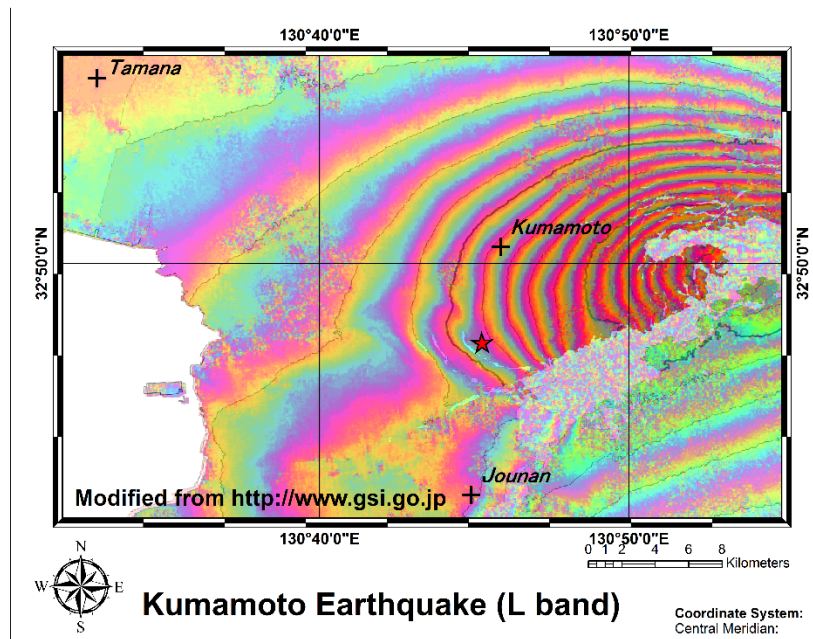
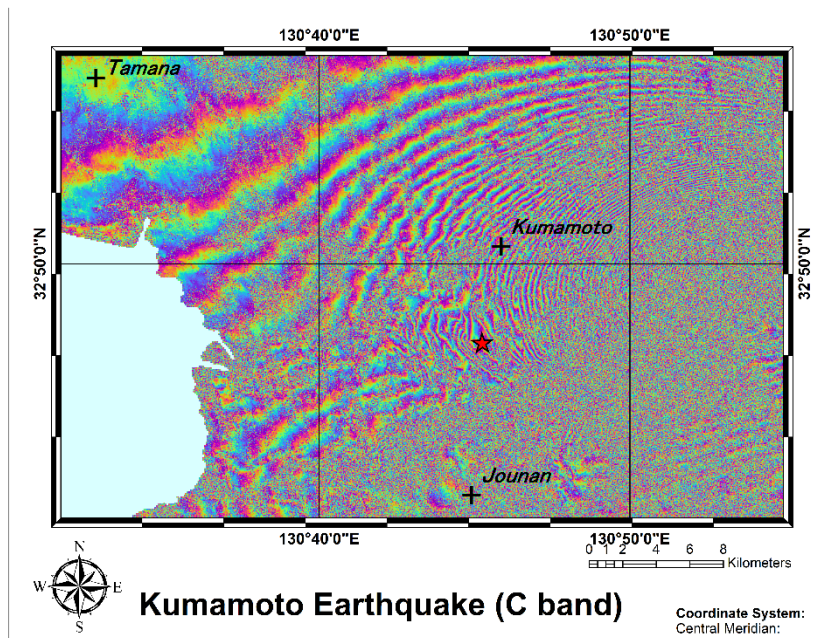


Figure 2: Result of an analysis of the L-band and C-band centering on the epicenter of the Kumamoto earthquake

In Figure 2, we can see rainbow-colored variations on the line segment between Kumamoto and Tamana on the map; variations of the digital value can also be seen. In Figure 4(a), the phase differences of the L-band and the C-band are displayed in rainbow color on the line segment that connects from Tamana to Kumamoto.



(a) Phase differences in the L-band around the epicenter



(b) Phase differences in the C-band around the epicenter

Figure 3: Phase differences around the epicenter (red star) and in Kumamoto and Tamana

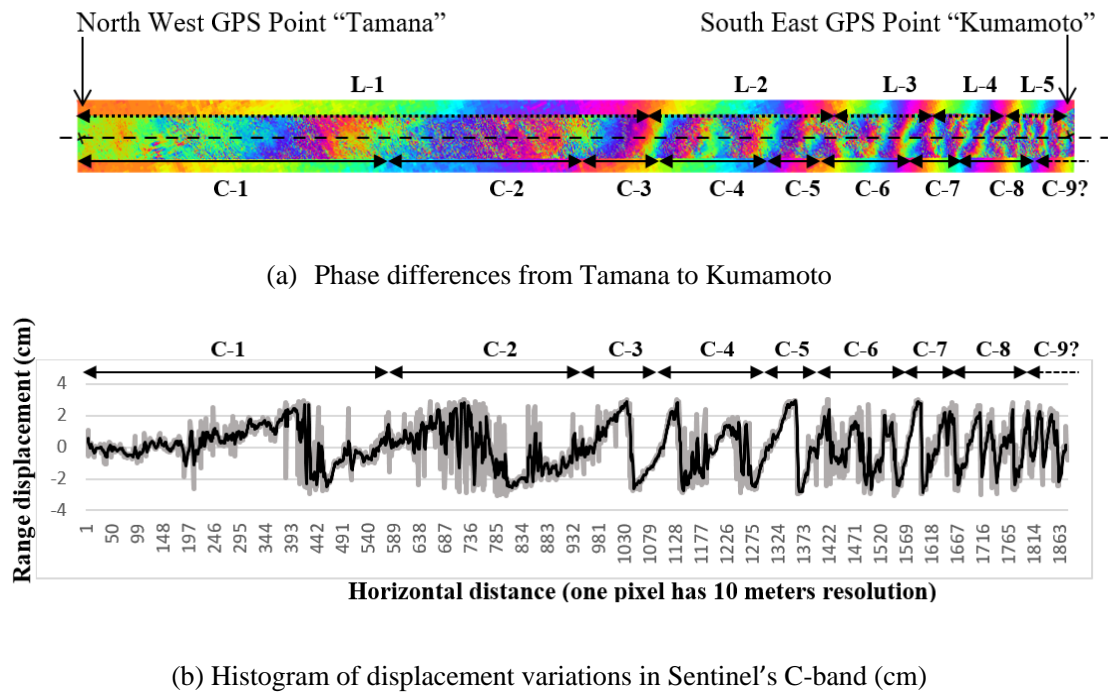


Figure 4: Phase differences around the epicenter from Tamana and to Kumamoto

Circles representing the phase difference are shown as L-1, L-2, and so on for the L-band and as C-1, C-2, and so on for the C-band. Moreover, Figure 4(b) can also be expressed as a digital value as shown in Figure 4(a), which is a histogram for only the C-band of the Sentinel satellite data. Therefore, the difference of a circular term between the L-band and the C-band is proportional to the ground resolution interval of a wavelength. Therefore, the displacement attributed to the natural earthquake with a weak seismic wave would be best understood by using the C-band rather than the L-band. In section 3, we have provided an analysis of the displacement in a nuclear test site of North Korea using the C-band.

(2) Phase unwrapping processing

The phase differences obtained by InSAR data analysis generate rainbow-colored images. When processing data using the SNAP software, the results were expressed as rainbow-colored phase picture images, which draw an equipotential contour as well. However, the rainbow-colored variations (or phase differences) were converted into actual displacements. This is called phase unwrapping processing. Besides, the image data obtained from this processing are named the unwrapped phase. This study investigates the phase unwrapping approaches by using SNAPHU, a software used exclusively for Unix. Figure 5 indicates that the areas surrounding the red star have become considerably complex by diastrophism. The analysis shows that the displacements caused by the Kumamoto earthquake range from -25 cm to $+211$ cm and occurred not only in areas surrounding the epicenter but also in wider areas in the Kumamoto Prefecture. Thus, phase unwrapping processing can show diastrophism in an intelligible way.

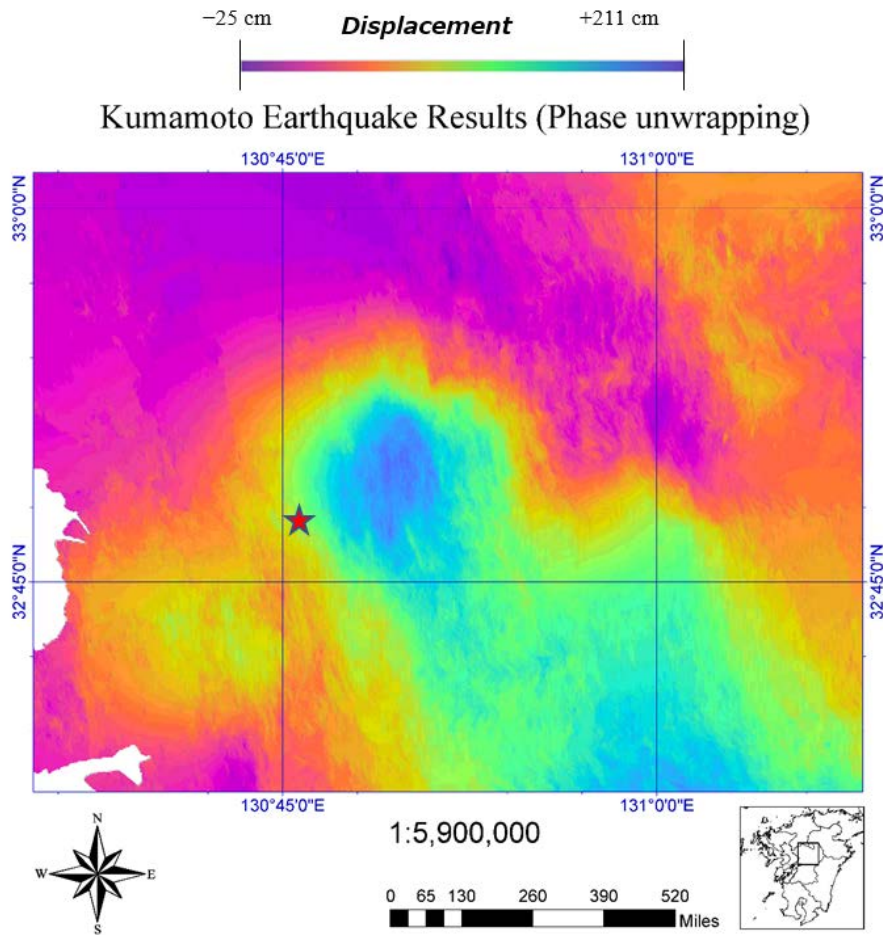


Figure 5: Displacement caused by the Kumamoto earthquake (with phase unwrapping)

4 Displacement model and discussion

Then, how much correspond this result (Figure 5) with GPS measured data in perpendicular direction. And how we can estimate the movement of earth surface with previous research. Figure 6 shows relationship between calculated with phase unwrapping and in-situ data using GPS instrument.

Generally, in order to guarantee the model verification, used data was split into a calibration area and a verification area. In this paper, however calibration and verification data were used as a same data. The reason why in-situ data of all Kumamoto area was small amount with only 9 points of GPS in around earthquake area. Since the relationship between calculated and in-situ displacement data is linear, the estimate model to derive displacement is as the follows:

$$D = -0.3114x + 10.599$$

where D is displacement, x should be calculated data with phase unwrapping.

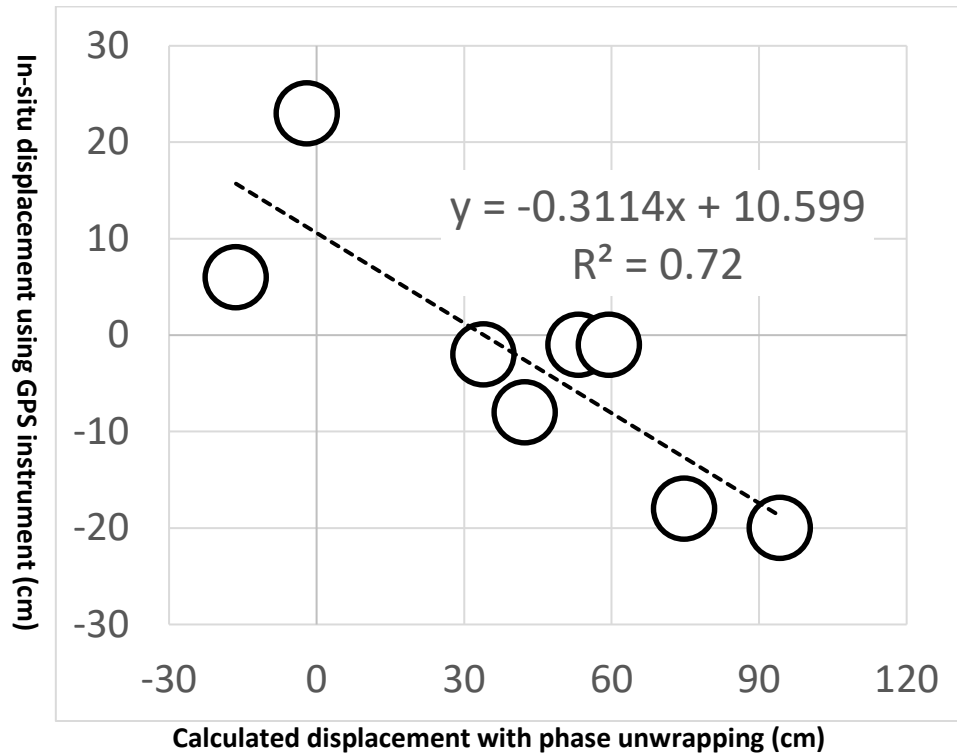


Figure 6: Displacement-GPS measured data graphs including the best fit regression lines plotted by the equations shown as a displacement estimate model.

The general fit of the models was calculated as the root mean square deviation (RMSD), which describes the mean deviation of the estimated values, in the unit of measure used on the input data (cm). The RMSD on the test area was 6.8 with an R^2 of 0.72.

References

1. Massonnet, D., and K.L. Feigl. 1998. "Radar Interferometry and Its Application to Changes in the Earth's Surface." *Reviews of Geophysics* 36 (4):441–500. <https://doi.org/10.1029/97RG03139>.
2. Zebker, H.A., P.A. Rosen, R.M. Goldstein, A. Gabriel, and C.L. Werner. 1994. "On the Derivation of Coseismic Displacement Fields Using Differential Radar Interferometry: The Landers Earthquake." *Journal of Geophysical Research* 99 (B10):19,617–19,634.
3. Zebker, H.A., P.A. Rosen, and S. Hensley. 1997. "Atmospheric Effects in Interferometric Synthetic Aperture Radar Surface Deformation and Topographic Maps." *Journal of Geophysical Research B: Solid Earth* 102 (B4):7547–63.
4. Dore, N., J. Patruno, E. Pottier, and M. Crespi. 2013. "New Research in Polarimetric Sar Technique for Archaeological Purposes Using ALOS PALSAR Data." *Archaeological Prospection* 20 (2):79–87. <https://doi.org/10.1002/arp.1446>.

Edge Extraction Algorithm for Road Markings Based on Single-Frame Image and Sparse Point Cloud

LIANG Qice¹ HUANG He¹ YI Pengjun² LUO Dean¹

¹ Beijing University of Civil Engineering and Architecture, Beijing 102616, China

² Beijing Survey and Design Research Institute Co. LTD , Beijing 100038, China

Abstract: Road markings occupy an important position in an intelligent, high-precision map feature library. Because advanced maps have high requirements for data accuracy, dense lidar point cloud data are usually used to extract road markings. However, the high price of high-threaded lidar and the huge amount of point cloud data are significant challenges in this domain. This study proposes a road marking edge extraction algorithm based on the fusion of a single-frame image and a sparse point cloud. The algorithm first extracts the edge and internal point coordinate information of road markings from the image and point cloud, respectively. Then, it uses the calibration parameters of the camera and lidar to register the image and the point cloud. Next, the edge points and the internal points are mutually verified to eliminate false detection data. Finally, geometric correction is performed on the road marking edge data to obtain the final plane coordinates. The height of the edge points is obtained by interpolation. We verify the performance of the algorithm and demonstrate that it can accurately and efficiently extract the edges of road markings and thus provide a new scheme for the automatic extraction of road markings.

Keywords: road markings; single-frame image; sparse point cloud; geometric correction

1. Introduction

With the advancement of artificial intelligence, cloud computing, and intelligentization of the automobile industry, high-precision maps have received widespread attention^[1-2]. They are a key factor for future intelligent travel. They contain a large amount of auxiliary information, such as lane lines and geographic objects around the road, which can help autonomous vehicles reduce the number of objects recognized and improve the accuracy of identifying relevant elements of the map. To achieve L3 level and above autonomous driving, high-precision maps are an indispensable requirement^[3]. As an important feature mark on the road, road markings provide valuable guidance to drivers and pedestrians. They are also the source of information and attributes such as road network data, lane network data, and some safety auxiliary data in high-precision maps^[4], so their accuracy is required to reach centimeter level. At present, the construction of road markings usually involves a vehicle-mounted lidar to collect high-density point cloud data, which is then extracted through automated methods. Guan Haiyan et al.^[5] extracted roads through slope and height difference thresholds, inserted pavement points into the geo-referenced intensity image using the extended inverse distance weighting method, and finally performed dynamic multi-threshold³ segmentation on the geo-referenced intensity image to

*Qice Liang, China, Beijing University of Civil Engineering and Architecture, 1181208223@qq.com

obtain road markings. Gao Yang et al. ^[6] used the coordinate, RGB, intensity, and other attribute information of the point cloud data to automatically extract road markings using the gray difference method, the intensity difference method, and the dynamic grid density method. Mario Soilán et al. ^[7] applied machine learning to

segment, extract, and classify common road markings. Fan Wen et al. ^[8] used the color, spatial neighborhood, and elevation of road markings to automatically classify point cloud data and extract road markings. Fang Lina et al. ^[9] used a combination of multiple models to enhance the difference in the reflection intensity between the ground and the marking point cloud; they also merged the shape, structure, and semantic information of the solid line marking to realize the solid line traffic sign in the vehicle laser point cloud along with accurate extraction and identification of lines. Yue Pan et al. ^[10] generated geographic reference images to extract road markings based on the intensity, elevation, and point density of the point cloud and used the images to construct a road marking classification scheme. They then used model matching to correctly classify the road markings. In the process of collecting the high-density point cloud data used in the above methods, the required high-threaded lidar equipment is expensive, and the amount of generated point cloud data is huge, resulting in low production efficiency of high-precision maps and complex and difficult updating. Therefore, low-cost low-threaded lidar enters the public's vision, but because its collection point cloud is sparse, the road marking error extracted by the above method is relatively large.

In response to the above problems, this study proposes a new road marking edge extraction algorithm that combines single-frame images and sparse point clouds so that mobile measurement vehicles equipped with low-thread lidar can extract high-precision and complete road markings with high performance and efficiency. This algorithm first extracts the edge points of road markings from the images based on the gray-scale difference method and extracts the internal points of the road markings from the sparse point cloud based on the intensity difference method. The image and point cloud are compared according to the calibration parameters of the camera and lidar. Using statistical filters, we verify and eliminate the false detection data of edge points and internal points. Finally, the algorithm combines geometric correction and interpolation to fit the height to realize point cloud conversion and obtain the edge points of road markings from two-dimensional pixel coordinates to three-dimensional point cloud coordinates.

2 Research method

This experiment uses the road data in the KITTI dataset and replaces the sparse point cloud data with a single frame of point cloud data to extract road markings. The specific images and point cloud data used are shown in Figure 1, the red box selection area is the guide arrow for the extraction. The single-frame image resolution is 1242*375 pixel, and the single-frame point cloud data have a total of 124,210 data points.

The proposed method of edge extraction of road markings that combines single-frame images and sparse point clouds has the following main steps: (i) Use images to extract road

*Pengjun Yi, China, Beijing Survey and Design Research Institute Co. LTD, 245935417@qq.com

*He Huang, China, Beijing University of Civil Engineering and Architecture, huanghe@bucea.edu.com

markings edge points; use point clouds to extract road markings internal points, road markings edge points, and internal points to verify each other; (ii) eliminate errors; (iii) perform geometric correction on the edges of road markings, and calculate elevation by interpolation and fitting.

The specific technical process is shown in Figure 2.

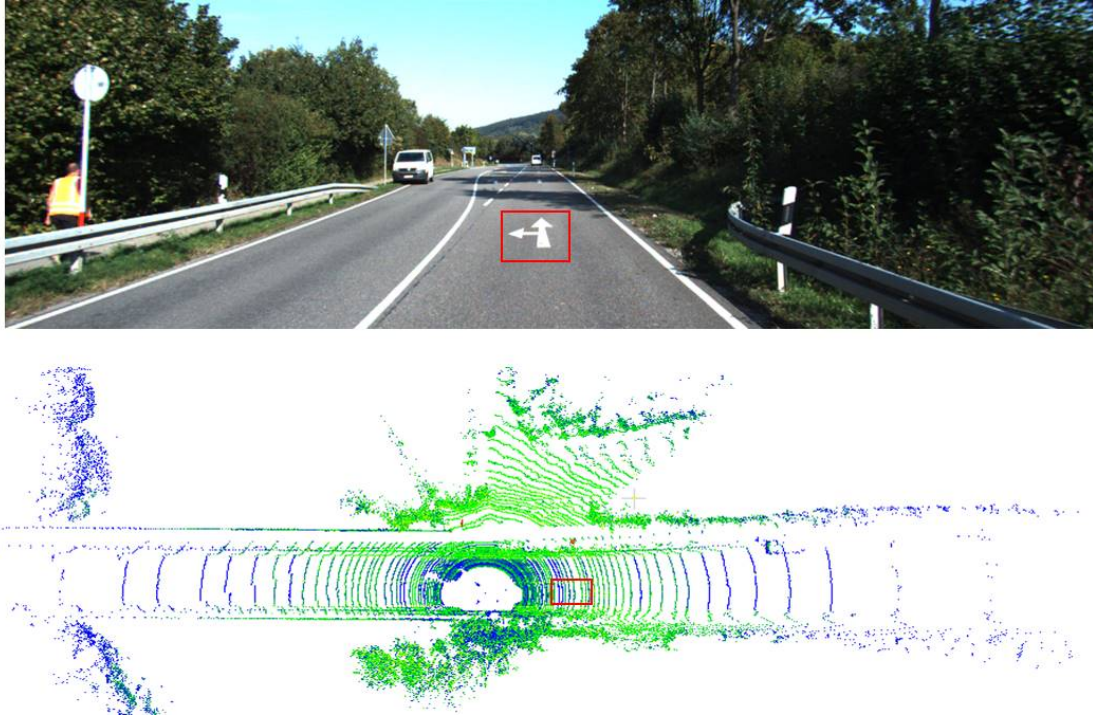


Fig. 1 Single-frame image and single-frame point cloud data used in this study

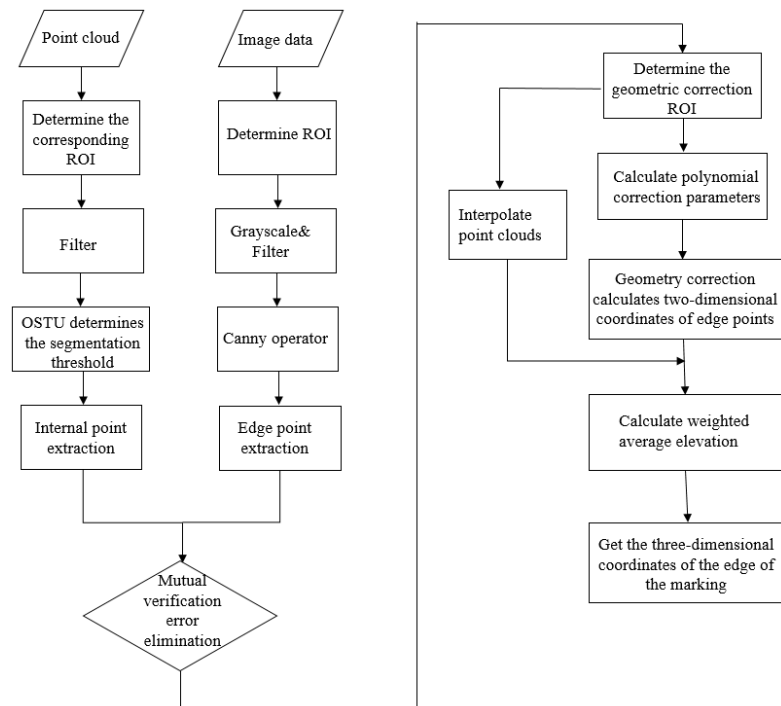


Fig. 2 The Technical Process of Road Marking Edge Extraction in This Paper

3. Road marking edge extraction steps and experiments

3.1 Image extraction of edge points

The image-based road marking edge points are extracted using the gray difference method [11,12]. To eliminate the interference and noise for road marking detection and increase the calculation efficiency of the algorithm, the image is first divided into the Regions of interest (ROI) based on the color difference between the road markings and the road background. The weighted average method is used to grayscale the image. The grayscale function is

$$g = 0.229R + 0.587G + 0.114B, \quad (1)$$

where g is the gray value of the gray image, and R , G , and B are the values of each channel in the color image.

To smooth the noise points generated during the gray-scale processing, the image needs to be filtered. Since the ROI is selected as the near field of view, the effect of Gaussian filtering is better than that of mean filtering and median filtering [13], as it can better retain edge information while removing noise. Finally, the canny operator is used to detect and extract the road edges of the road markings. The extraction results are shown in Figure 3.



Fig. 3 Image-based Road Marking Edge Extraction

3.2 Point cloud extraction of internal points of road markings

Based on the point cloud, the internal points of road markings are extracted using the intensity difference method [14]. In the structured road environment, because the road markings generally use yellow or white coatings, the echo intensities of the laser lidar sensor scanning of the road surface and the road markings are quite different. It can be divided according to the difference of echo intensity between road marking and road surface. To avoid the influence of roadside trees, buildings, and other extraneous objects on road marking detection and to improve calculation efficiency, the point cloud is divided into ROIs. According to the camera calibration parameters and the rotation matrix and translation matrix jointly calibrated by lidar and camera,

the point cloud is registered with the image and the point cloud is projected onto the image. The ROI of the point cloud is confirmed according to the ROI range on the image.

$$\begin{bmatrix} u \\ v \\ 1 \end{bmatrix} = \begin{bmatrix} f_x & 0 & u_0 & 0 \\ 0 & f_y & v_0 & 0 \\ 0 & 0 & 1 & 0 \end{bmatrix} \begin{bmatrix} R & T \\ \bar{0} & 1 \end{bmatrix} \begin{bmatrix} x \\ y \\ z \\ 1 \end{bmatrix}, \quad (2)$$

where u_0, v_0 are the image centers; f_x, f_y are the normalized focal length on the x-axis and y-axis; R is the rotation matrix; T is the translation matrix; x, y, z are the point cloud coordinates; and u, v are the pixel coordinates.

The lidar generates some noise points during the scanning process, which affect the final interpolation fitting calculation of the elevation. Therefore, the statistical filtering method is used to remove obvious outliers. The results are different due to the different calculation methods of the echo intensity of each lidar device. To increase the applicability and robustness of the algorithm, the Otsu algorithm is used as the image processing method (maximum between-class variance method, also known as Otsu's method) to automatically determine the best segmentation threshold. First, the point cloud is divided into two parts: the background and the target according to the point cloud echo intensity; then, the inter-class variance of the two parts of the point cloud is calculated. When the inter-class variance is the largest, it is the optimal segmentation threshold t , and the point cloud exceeding the threshold t is the internal point of the road marking.

The result is shown in Fig. 4. The red circle is the point inside the road where the echo intensity is greater than the threshold t . The specific calculation formula of the Otsu method is as follows:

$$\text{Percentage of background point cloud: } \omega_1 = \frac{N_1}{\text{Sum}} \quad (3)$$

$$\text{Proportion of point cloud of target part: } \omega_2 = 1 - \omega_1 = \frac{N_2}{\text{Sum}} \quad (4)$$

$$\text{The average intensity value of the background point cloud: } \mu_1 = \frac{\sum_{i=M_{\min}}^t i * Pi}{\sum_{i=M_{\min}}^t Pi} \quad (5)$$

$$\text{The average intensity value of the target point cloud: } \mu_2 = \frac{\sum_{i=t+1}^{M_{\max}} i * Pi}{\sum_{i=t+1}^{M_{\max}} Pi} \quad (6)$$

$$\text{Average intensity of all point clouds: } \mu = \mu_1 * \omega_1 + \mu_2 * \omega_2 \quad (7)$$

$$\text{Between-class variance: } g = \omega_1 * (\mu - \mu_1)^2 + \omega_2 * (\mu - \mu_2)^2 = \omega_1 * \omega_2 * (\mu_1 - \mu_2)^2 \quad (8)$$

In the formula, Sum is the total number of point clouds; N_1 , N_2 are the number of background and target point clouds; M_{min} , M_{max} are the minimum and maximum intensity values in the point cloud data.

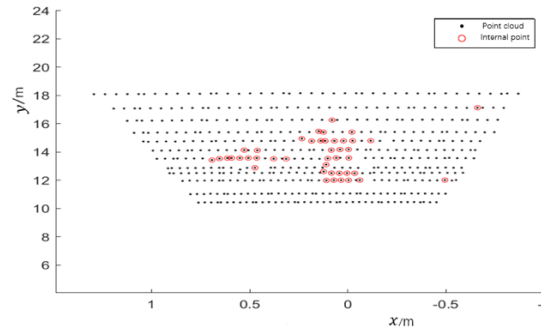


Fig. 4 Extraction of Points Inside Road Markings Based on the Point Cloud

3.3 Screening and eliminating false detection data

Image extraction of road marking edges and point cloud extraction of internal points of road markings may result in mis-detected and erroneous data. It is necessary to verify the edge points and internal points and filter out the mis-detected data. Based on the principle of statistical filtering, we use edge points to filter internal points and use internal points to filter edge points. The specific principle is as follows: project the internal points of the road marking to the pixel coordinates of the image and calculate the average pixel distance $d_{average}$ between it and the nearest n edge points of the road marking. In the same way, calculate the edge points of all road markings and their nearest n edge points. The average pixel distance $D_{average}$ of the points inside road markings is shown in Figure 5. Set an appropriate threshold L according to the width of the road markings and the distance between the adjacent lines of the lidar on the road surface and delete the points that exceed the threshold L so that some false detection data can be filtered out. The result is shown in Figure 6.

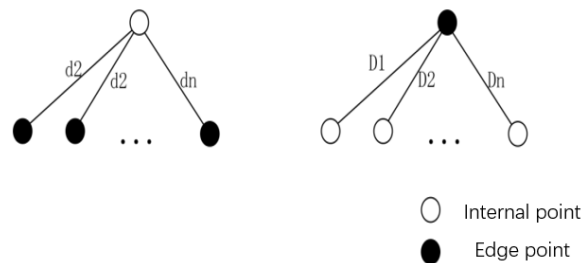


Fig. 5 Schematic Diagram of Mutual Verification of Edge Points and Internal Points

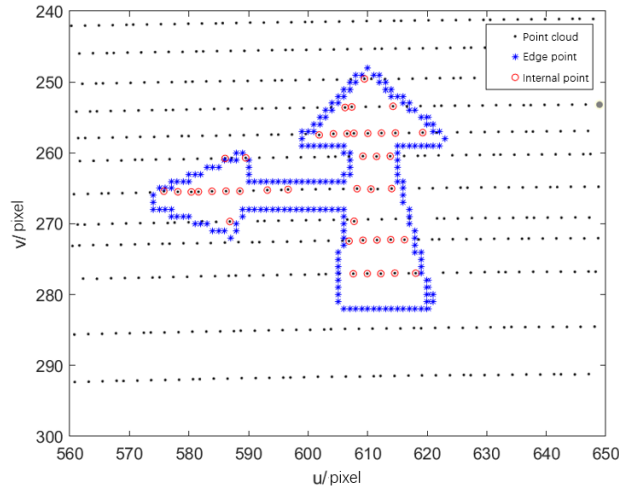


Fig. 6 Results of Screening and Rejection of False Detection Data

3.4 Geometric correction

Geometric correction is the process of eliminating or correcting the geometric errors of the image. It is the conversion of the image from two-dimensional to two-dimensional, as shown in Figure 7. The coordinates of the point cloud are three-dimensional and cannot be directly geometrically corrected. However, a single road marking area is very small and can be assumed to be a plane, so the point cloud can be orthographically projected to convert it into a two-dimensional plane. Because the previously selected ROI area is too large, the geometric correction error is also large. To address this, the geometric correction area is reselected according to the edge points and internal points of the road markings. Then, we use the polynomial correction method in the digital image geometric correction method and use the point cloud data and pixel coordinates in the area to calculate the polynomial correction parameters. Finally, the pixel coordinates of the edge points of the road markings are taken into the polynomial correction equation and their two-dimensional coordinates in the lidar coordinate system are calculated. The result is shown in Figure 8.

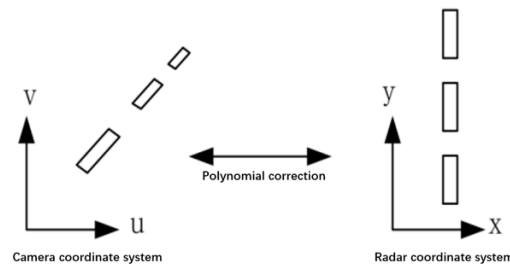


Fig. 7 Geometric Correction Diagram

The polynomial correction equation is

$$\begin{cases} u = a_0 + (a_1x + a_2y) + (a_3x^2 + a_4xy + a_5y^2) \\ v = b_0 + (b_1x + b_2y) + (b_3x^2 + b_4xy + b_5y^2) \end{cases}, \quad (9)$$

where x , y are the coordinates of the point cloud in the correction area in the lidar coordinate system; u , v are the pixel coordinates of the point cloud in the correction area in the image coordinate system; and a_i , b_i are polynomial parameters.

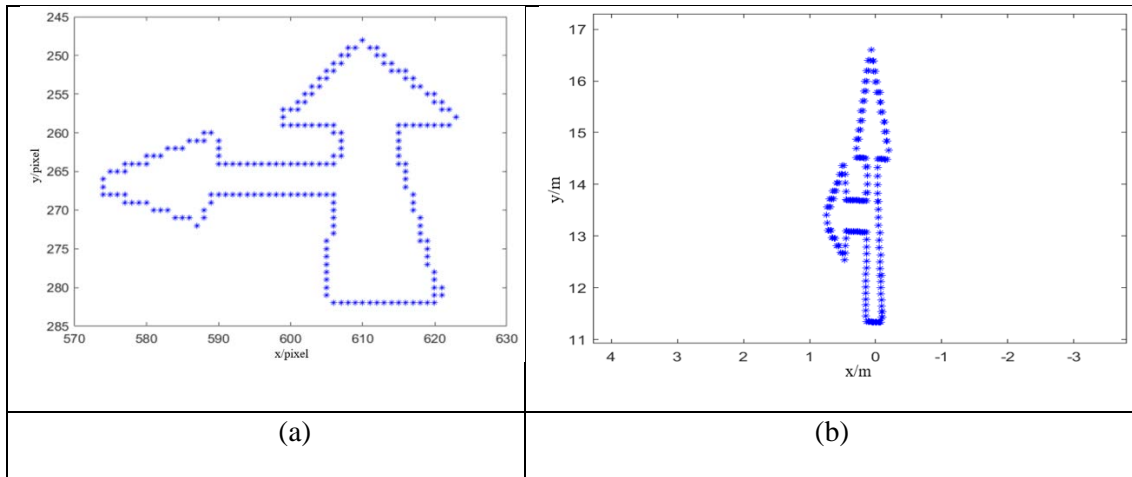


Fig. 8 (a) Edge points of road markings before geometric correction. (b) Edge points of road markings after geometric correction.

3.5 Elevation fitting of edge points

After geometric correction, the edge points of the road markings only have two-dimensional coordinates. Their elevations need to be fitted and calculated. Because the point cloud data is relatively sparse, the elevation error of directly calculating the edge points of the road markings is large. Therefore, the point cloud data need to be subjected to the triangle-based cubic interpolation method so that the interpolation result is smoother and more in line with the actual situation. The steps are as follows. Find the four interpolation points C1, C2, C3, and C4 around the two-dimensional coordinates of the edge point D of the marking and then calculate the height of the edge point of the road marking according to the height of these four interpolation points using the distance-weighted average. Thus, the road markings' three-dimensional coordinates of the edge point are obtained. The weighted average fitting elevation diagram is shown in Figure 9.

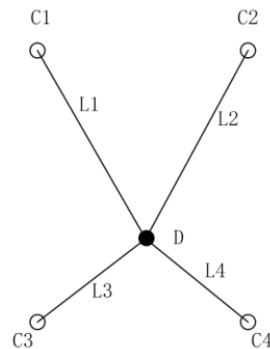


Fig. 9 Fitted Elevation Diagram

$$h_D = \frac{h_1 L_1 + h_2 L_2 + h_3 L_3 + h_4 L_4}{L_1 + L_2 + L_3 + L_4}, \quad (10)$$

where h_D is the elevation of the edge point D of the road marking; h_1, h_2, h_3, h_4 are the elevations of the four interpolation points C1, C2, C3, C4; L_1, L_2, L_3, L_4 are respectively the distances of four interpolation points C1, C2, C3 and C4 to the edge point D of the road marking.

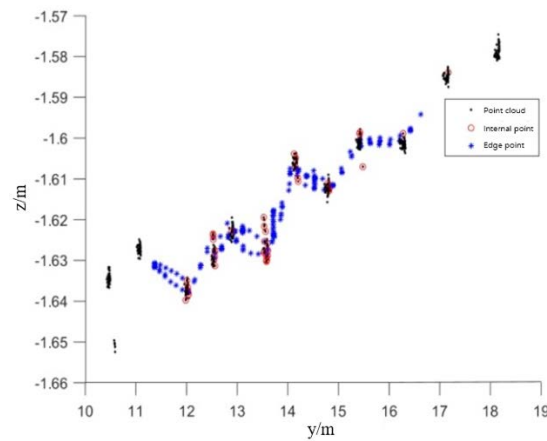
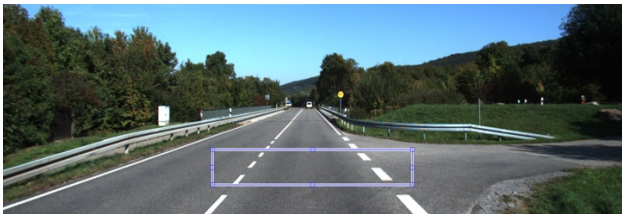


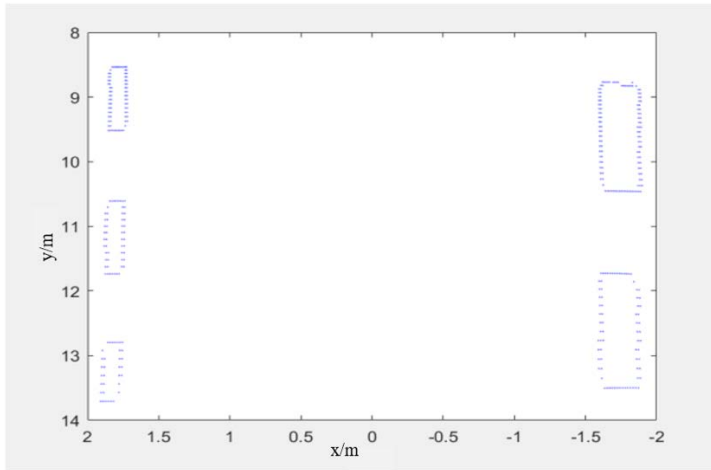
Fig. 10 Results of Elevation Fitting

4 Result analysis and accuracy verification

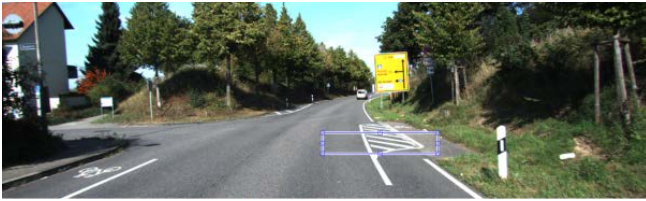
Using the proposed algorithm, the edge points of different types of road markings such as dashed lines and diversion areas were extracted. The extraction results are shown in Figure 11.



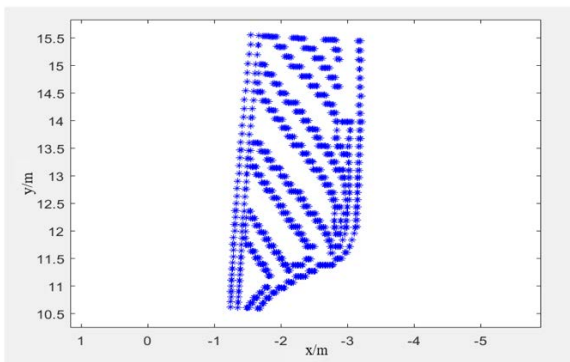
(a)



(b)



(c)



(d)

Fig. 11 (a) Dashed road marking ROI. (b) Extraction results of edge points of dashed road markings. (c) Road marking ROI in diversion area. (d) Extraction results of edge points of road markings in diversion area.

To evaluate the accuracy of the road marking edge extraction algorithm, the evaluation was conducted from the following two aspects:

1) Image-based internal verification: Project the extracted road marking edge data onto the image according to formula (2) and compare the projected pixel coordinates with the road marking edge data extracted based on the original image (Figure 12). Verify the pixel difference

between the edge points of the road markings before and after geometric correction and elevation fitting, as shown in Figure 13.

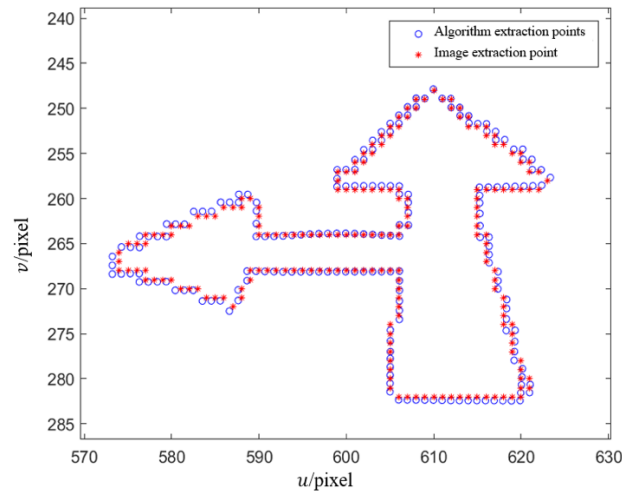


Fig. 12 Comparison Between The Algorithm and Image Extraction Edge Points

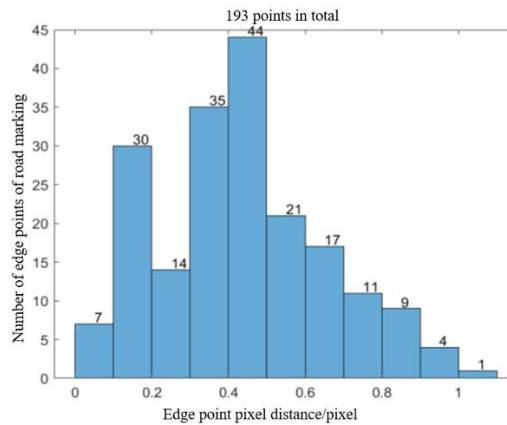


Fig. 13 Edge Point Pixel Difference Distribution Map

2) External verification based on the point cloud: Compare the method in this paper with the traditional method of extracting road markings from the high-density point cloud. First, use the 3D-NDT algorithm based on normal distribution transformation to match the point cloud to build a high-density point cloud map. The algorithm uses a statistical model to determine the optimal parameters for point cloud matching and mapping; it has good robustness and high efficiency [15]. Then, calculate the high-density point cloud data according to the Otsu algorithm; determine the echo intensity threshold between the road marking and the road surface; and extract the internal points of the road marking according to the threshold, as shown in Figure 14. The results are compared and verified with the road marking width extracted in this paper, as shown in Figure 15.

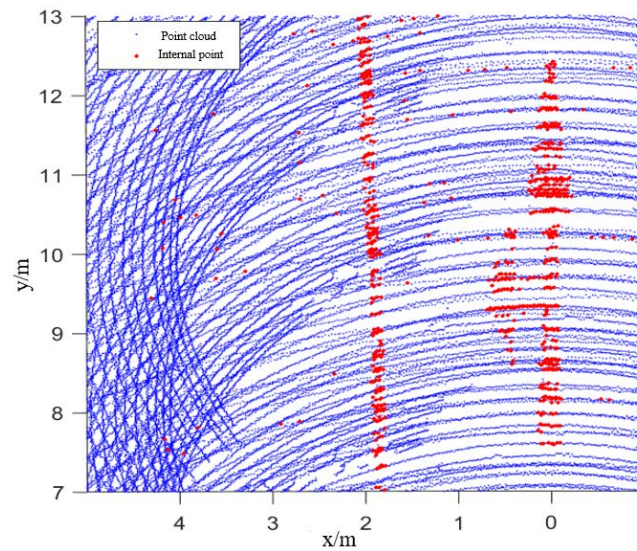


Fig. 14 Interior Points of Road Markings

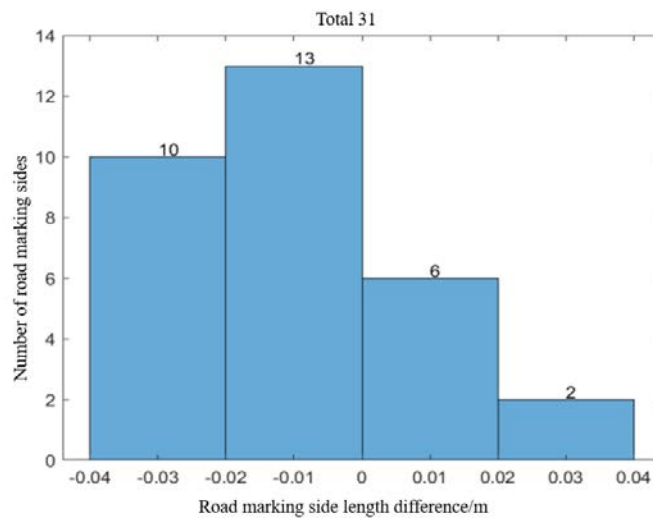


Fig. 15 Distribution Map of Side Length Difference of Road Marking

Table 1 shows the accuracy analysis table of the comprehensive extraction results based on image-based internal verification and point cloud-based external verification.

Tab.1 Accuracy Analysis Table for the Extracted Results

Verification index	Average difference/pixel	pixel	Average side length	Average relative error of side length
Precision	0.431	-0.011		5.6%

It can be seen from Table 1 that the edge points of road markings change little before and after geometric correction and elevation fitting. Compared with the road markings extracted from

the high-density point cloud data, the average side length difference of this method is -0.011 meters and the average relative error of side length is 5.6% . It takes an average of 6.39 s to extract the edge points of a single road marking through the algorithm in this study, while the traditional method has a large amount of point cloud data and therefore takes a long time to read the point cloud, amounting to an average time 16.66 s to extract a single road marking. The results show that the road marking extraction algorithm of this study, which combines single-frame images and sparse point clouds, can quickly, accurately, and effectively extract the edges of road markings.

5 Conclusion

To address the research and practical challenges posed by the large volume of high-precision map point cloud data and high cost of high-threaded lidar sensor, this study proposes a road marking extraction algorithm that combines a single-frame image and sparse point cloud and innovatively uses image recognition of road markings. The advantages of high accuracy of both edges and lidar point cloud coordinates provides the data for subsequent high-precision map road marking data expression. Overall, this is a new solution for road marking extraction. However, this method is susceptible to the influence of slope in the orthographic projection of the point cloud data. Further optimization is warranted in the future.

References

- 1) Jo K, Sunwoo M. Generation of a Precise Roadway Map for Autonomous Cars[J]. IEEE Transactions on Intelligent Transportation Systems, 2014,15(3):925-937.
- 2) Shim I,Choi J,Shin S,et al. An Autonomous Driving System for Unknown Environments Using a Unified Map[J]. IEEE Transactions on Intelligent Transportation Systems,2015,16(4): 1999-2013.
- 3) Liu Jingnan , Zhan Jiao , Guo Chi , Li Ying , Wu Hangbin , Huang He. Data Logic Structure and Key Technologies on Intelligent High-precision Map [J] .Acta Geodaetica et Cartographica Sinica, 2019, 48 (8): 939-953.
- 4) Liu Jingnan, Wu Hangbin, Guo Chi, Zhang Hongmin, Zuo Wenwei, Yang Yan. Progress and Consideration of High Precision Road Navigation Map [J] . Engineering Sciences, 2018,20 (02): 99-105.
- 5) Haiyan Guan,Jonathan Li,Yongtao Yu,Cheng Wang,Michael Chapman,Bisheng Yang. Using mobile laser scanning data for automated extraction of road markings[J]. ISPRS Journal of Photogrammetry and Remote Sensing,2014,87.
- 6) Gao Yang, Wang Liuzhao, Li Ming. Study on the Extraction Methods of Road Signs Based on Vehicular Color Laser Point Cloud [J] .Bulletin of Surveying and Mapping, 2016 (04): 28-32.
- 7) Mario Soilán,Belén Riveiro,Joaquín Martínez-Sánchez,Pedro Arias. Segmentation and classification of road markings using MLS data[J]. ISPRS Journal of Photogrammetry and Remote Sensing,2017,123.
- 8) Fan Wen, He Elong, Li Tianqi, Sun Jie. Lane Marking Extraction for MLS Data Based on Space-spectral Feature, 2018 (08): 97-101.

- 9) Fang Lina , Huang Zhiwen , Luo Haifeng , Chen Chongcheng. Solid Lanes Extraction from Mobile Laser Scanning Point Clouds [J] . Acta Geodaetica et Cartographica Sinica, 2019,48 (08): 960-974.
- 10) Pan, Y., Yang, B., Li, S., Yang, H., Dong, Z., and Yang, X.: Automatic Road Markings Extraction, Classification and Vectorization from Mobile Laser Scanning Data, Int. Arch. Photogramm.Remote Sens. Spatial Inf. Sci., XLII-2/W13, 1089-1096, <https://doi.org/10.5194/isprs-archives-XLII-2-W13-1089-2019>, 2019.
- 11) Cao Chenjie, Wang Xiali, Zhao Jiaxing, Wang Lihong. Road Traffic Marking Recognition Method Based on CANNY Algorithm [J] .Information Technology and Network Security, 2019,38 (10): 78-82 + 92.
- 12) Liu Yanbin. Research on Lane Line Detection Based on Structured Road [J] .Transportation Science and Technology, 2019 (04): 117-121.
- 13) Wang Zhen. Research on Lane Detection Algorithm in Intelligent Driving [D] .Anhui Polytechnic University, 2019.
- 14) Mao Yinrui, Chen Yuren, Liu Yangdong. Study on Road Marking Extraction Method Based on Mobile LIDAR Point Cloud [J] . Journal of Highway and Transportation Research and Development, 2019,36 (07): 127-135.
- 15) Zhang Tianxi, Zhou Jun, Liao Huali, Yang He.Simutaneous Localization and Mapping Strategy of Graph Optimization Based on Three-Dimensional Laser [J] .Laser & Optoelectronics Progress, 2019, 56 (20): 309-315.

3-D Model Reconstruction of Buildings by integrating Oblique Photography and Terrestrial LiDAR

Teng-Fei Yu¹ He Huang¹

¹ School of Geomatics and Urban Spatial Informatics, Beijing University of Civil Engineering and Architecture, Beijing 102616, China.

ABSTRACT: With the continuous advancement of geographic information technology, the smart city has become an inevitable trend. Three-dimensional (3-D) models are an excellent way for introducing important information about smart cities to people. However, some particular characteristics derived from irregular urban structures can constrain the use of some technologies for 3-D data collection. Oblique photography has the advantages of high efficiency and rich information, and it also playing an increasingly important role in the construction of smart city. However, the accuracy of the model generated by this technique affected by factors such as occlusion at the bottom of the building, which results in a 3-D real-world model with poor accuracy. Aiming at the demand of high precision and refined real-life reduction of a 3-D real-world model for smart city, this research paper proposes a working methodology for model reconstruction of buildings. This methodology is based on the combined use of terrestrial laser scanning and oblique photography techniques, which complement each other. Through the combination method, complete point cloud information of different perspectives of the building can be acquired, then build high-precision building models through point cloud data fusion technology which has obvious advantages in constructing a high-precision and good-recovering 3-D real-life model. The experimental results showed that, the Medium error of the constructed 3-D real-world model plane is 0.058 m , and Medium error in elevation is 0.038 m , the method is feasible in the construction of a 3-D model of urban architecture.

Keywords: smart city; 3-D model; oblique photography; terrestrial laser scanning; data fusion

1.Introduction

In recent years, with the development of economy, the urbanization process is accelerating constantly. Meanwhile, there are still many problems in the process of managing the city, so the smart city has become a means of effectively managing the city [1]. In the formation and development of smart cities, the most important goal is to obtain accurate geographic information. By building high-precision 3-D models and performing 3-D spatial analysis, in this way, the city can become smarter. The acquisition technology of 3-D spatial information is developing very rapidly. In order to support the needs of smart cities, refined 3-D urban reconstruction is an important basic work, and it is necessary to

introduce a singular 3-D building model with complete and detailed information in 3-D urban reconstruction.

In the process of constructing the city's 3-D model, two new technologies, Unmanned Aerial Vehicle (UAV) oblique photogrammetry [2] and terrestrial LiDAR [3, 4], are used, and they play an increasingly important role in smart cities. The main benefit of the technologies is in fast data acquisition and high accuracy – several millimeters for Terrestrial Laser Scanner (TLS) [5] and several centimeters for UAV [6]. Although the UAV photogrammetry technology can quickly and efficiently acquire the image data of the target object and achieve complete 3-D real-time reconstruction, due to the limitation of the aircraft operation mode, it is impossible to completely obtain the relevant information of the lower part and the inside of the target. When the target structure is complicated or the terrestrial area appears to be occluded by other objects, the 3-D real-life model based on the UAV oblique photography technology will appear such as model distortion. This is also a hotspot and difficulty in this field. The terrestrial LiDAR can acquire high-precision point cloud data quickly, but when the top of the scanned target exceeds the maximum range of scanning, it will not be able to obtain point cloud information and even cause data loss. Either way, in cases where TLS or UAV are used separately, data shadows originate in areas which are obscured in the sensor's field of view [7].

In response to such problems, many scholars have conducted in-depth research on how to quickly and efficiently acquire spatial 3-D information and reconstruct its 3-D model. A large number of studies have conducted 3-D modelling in urban areas based uniquely on photogrammetric techniques [8], laser scanner techniques [9] or more recently, both combined. The study of oblique photography began in the 1990s [10]. During the last years a trend towards extending the study area in terms of quality and resolution [11] of the models evolved. The main problem facing this technology is how to realize multi-source data fusion to build a high-precision, high-authenticity 3-D model. Combined use of Terrestrial Laser Scanning and photogrammetric techniques is nowadays accepted as the most optimal solution for generating 3-D models in urban environments [12]. Literature [13] combined with 3-D terrestrial LiDAR and close-range photogrammetry to propose a method for automatically generating 3-D models of historical cities. In 2009, George Vosselman presents a semiautomatic building facade reconstruction approach, which efficiently combines information from terrestrial laser point clouds and close range images. A building facade's general structure is discovered and established using the planar features from laser data [14]. Hossam used the hybrid technique showed the optimum achieved accuracy for 3D digital documentation which has been established based on measuring scanned values, for example the enhancement obtained in accuracy reached its submit in hybrid technique by 80.1%, 66.4%, and 84.2% when surveying features point coordinates, lines and angles [15].

In order to improve the accuracy of the 3D model, this article brings up a method of the terrestrial LiDAR combined with UAV oblique photogrammetry to reconstruct the 3-D model of the building. Fusion of point clouds by manual registration and Iterative closest point (ICP) algorithm [16], and the building is modeled finely. Through the experiment, the problem of distortion in part of the model caused by the data shadows is solved.

2. Materials and Methods

The combination of 3-D laser scanning technology and oblique photogrammetry technology can obtain complete information on the surface of the building and achieve high-precision 3-D modeling. The overall operation process is shown in Figure 1.

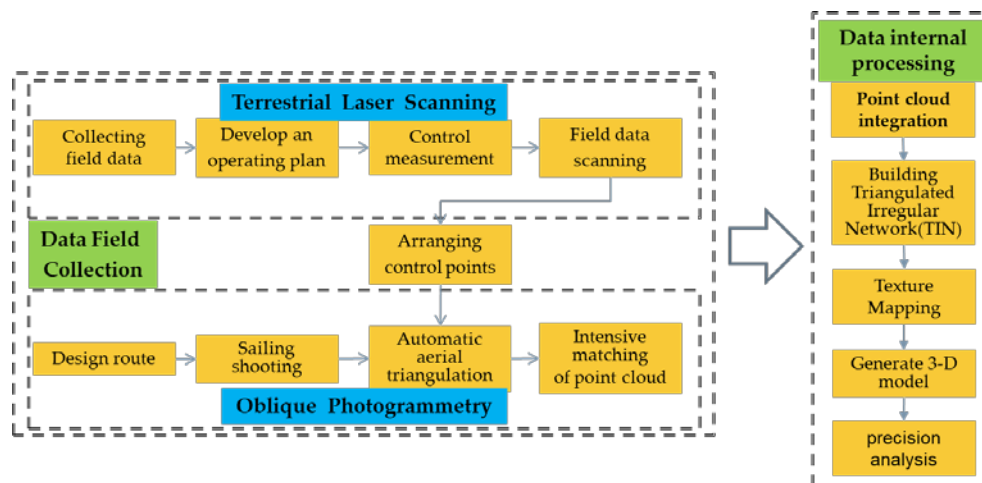


Fig. 1 Real-life 3-D reconstruction workflow based on the combination of oblique photography and terrestrial LiDAR technology

2.1 Method for Collecting Spatial Information

A wide range of image data can be acquired in a short time by tilt photography. However, due to the altitude of the UAV is high, it is easily obscured by vegetation or eaves, resulting in the lack of texture, even resulting in the inability to generate a complete encrypted point cloud during aerial triangulation. The terrestrial LiDAR technology can assist the oblique photogrammetry to repair the point cloud lost in the blind area. Therefore, Combination of the two technical methods can make their advantages complementary, not only improves efficiency, but also maintains image point cloud integrity, thus improving the fineness of the model [12].

2.1.1 UAV Oblique Photography

UAV has the characteristics of high mobility, flexibility, low-altitude flight, fast and safe. Therefore, it also plays an important role in the process of remote sensing image data acquisition as a new technical means. However, it also has many defects, such as limited image size, data shadow in the image, and high requirements for image overlap. As a revolutionary mapping technology, oblique photogrammetry technology has developed rapidly under the support of UAV technology, especially in the comprehensive and rapid construction of 3-D real-world models. It has important practical application value [17], UAV the combination of oblique photography and UAV is a research hotspot in the current surveying and mapping industry [18].

2.1.1.1 Terrestrial LiDAR

After the emergence of GNSS technology, Terrestrial LiDAR technology is playing an important role. The laser scanning technology also has a traditional manual single point measurement to automatically acquire data for the data acquisition method [19]. Compared with the traditional methods, the Terrestrial LiDAR technology can complete the acquisition without touching the measured object itself, and it has a high degree of automation. At the same time, this technical method also has the advantages of high accuracy and speed of measured data [20]. However, there are still some shortcomings in the application, such as scanning blind spots on the top of high-rise buildings and structures and low processing efficiency of post-processing software et al.

2.2 Fusion modeling technology based on multi-source data

By scanning buildings, the terrestrial laser scanner can obtain the point cloud data of the building directly. At the same time, using UAV equipped with digital cameras to build UAV platforms, collecting multi-angle data from buildings to capture high-precision image data. Then, Matching the same-named points in the image data by aerial triangulation method and image intensive matching algorithm, and Then, extract more feature points from the image data to build a dense point cloud data set.

Because of the large amount of point cloud data generated during the intensive matching process, this provides operability for the fusion of the LiDAR point cloud and the oblique photography dense point cloud. However, the image and laser point cloud are heterogeneous in nature. So there is a certain difficulty in automatic matching of the same name. Point cloud registration is an important part of the point cloud data processing process. The purpose is to convert the point clouds in different coordinate systems into the same coordinate system through registration, finally, to obtain a complete point cloud model of the building. Therefore, In order to achieve high-precision registration of image point cloud and laser point cloud, the method used in this paper is to perform coarse registration and fine registration.

2.2.1 Coarse Registration of Point Clouds

The coarse registration of the image point cloud and the laser point cloud is performed by manually selecting feature points manually. The point cloud coarse registration is to solve the two rotation solutions of the point cloud approximation. The equation is expressed in Equation (1):

$$p_t = R \cdot p_s + T \quad (1)$$

Where p_t and p_s represent the corresponding points in the target point cloud and the data source point cloud, and R 、 T are the rotation and translation matrices of the two point clouds solved. The point cloud coarse registration is mainly to provide an initial estimate for fine registration, reducing the time required for iteration in the fine registration process.

2.2.2 Fine Registration of Point Clouds

After completing the step of coarse registration of point clouds, in order to improve the accuracy of the point cloud registration, it is necessary to registration point cloud fine. Based on the curvature of the freeform surface, and to use ICP algorithm to accurately register point cloud . As shown in Figure (a) below, the blue point cloud and the orange point cloud are two different point sets. According to the correct corresponding points of the point set, the ICP algorithm performs relative transformation (rotation, translation, etc.) on the two different point sets , to achieve the fusion model of point clouds, the basic idea of the ICP algorithm is shown in Figure (b):

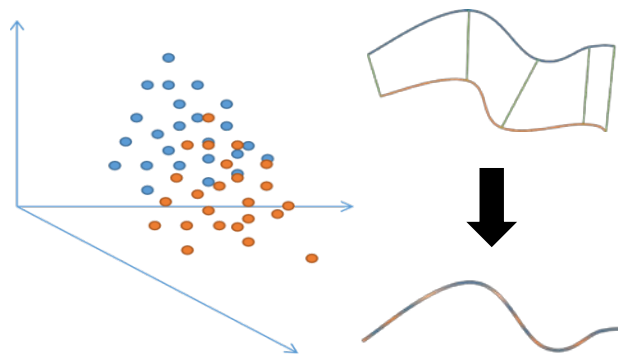


Fig. 2 Point cloud registration based on ICP algorithm.(a) Different points in the same coordinate system.(b) Registration process of point cloud.

The ICP algorithm uses a seven-parameter vector $X = [q_0, q_x, q_y, q_z, t_x, t_y, t_z]$ to represent the rotational and translation of the point cloud. Where $q_0^2 + q_x^2 + q_y^2 + q_z^2 = 1$ is fixed equation and P is the source point cloud, S is the target point cloud. and the distance function is:

$$d(P, S) = \min_{x \in X} \|x - P\| \quad (2)$$

The steps of the ICP algorithm are as follows:

Step 1: Set the initial seven parameter vector $X_0 = [1, 0, 0, 0, 0, 0, 0]^T$

Step 2: Where, P and S_i are different point cloud set, calculate their closest point in the corresponding point set;

Step 3: Where, X_{k+1} is parameter vector, to obtain the value through the registration process of the point set and the point set, and calculate d_k as the square sum of the distance;

Step 4: Where, P_{k+1} is a new point set, for point set P_{k+1} , Need to transform the point set P through the parameter vector to get . If the requirements in step 5 are not met and repeat the calculation in Step 2;

Step 5: Iterative stop when d_k is less than the preset threshold.

2.3 Method of precision analysis of fusion model

The total station can obtain accurate point information of the building as a true value by field measurement, and the 3-D model is decomposed into primitive points, lines, and the overall quality is evaluated by local precision.

2.3.1 Accuracy evaluation based on primitive points

According to the complexity of the real building, the corner points of the window and the edge points of the building are used as inspection corner points. n corner points were randomly selected in the corner points of the window in the building model, and the corner coordinate strings of the 3-D model are obtained as follows:

$$A_i(x_i, y_i, z_i), i \in [1, n]$$

The true corner coordinate string of the building corresponding to the model is:

$$B_j(x_j, y_j, z_j), j \in [1, n]$$

The distance difference $|A_i B_j|$ between the points is calculated by calculation:

$$|A_i B_j| = \sqrt{(x_j - x_i)^2 + (y_j - y_i)^2 + (z_j - z_i)^2} \quad (3)$$

Take the mean value a of the distance offset between the 3-D model point and the real point, that is, the accuracy value of the 3-D model primitive point:

$$a = \frac{1}{n} \sum_{i,j=1}^n |A_i B_j| \quad (4)$$

Then calculate the error of the n checkpoints in the three directions of an axis. The formula (5) is as follows:

$$\begin{aligned} m_x &= \pm \sqrt{\frac{\Delta_x \Delta_x}{n}} \\ m_y &= \pm \sqrt{\frac{\Delta_y \Delta_y}{n}} \\ m_z &= \pm \sqrt{\frac{\Delta_z \Delta_z}{n}} \end{aligned} \quad (5)$$

The following formula also exists in formula (5):

$$[\Delta\Delta] = \Delta_1^2 + \Delta_2^2 + \dots + \Delta_n^2 \quad (6)$$

$$\Delta_i = l_i - L \quad (i = 1, 2, \dots, n) \quad (7)$$

Where l_i is the observed value, L is the true value, Δ_i is the true error, and n is the number of checkpoints. The mid-error of the plane of the model is calculated from the medium error in the X direction and the Y direction. The formula (8) is calculated as follows:

$$m = \pm \sqrt{m_x^2 + m_y^2} \quad (8)$$

2.3.2 Accuracy evaluation based on primitive lines

(1) Offset c of Distance

Measure the two endpoints A_1 and A_2 of one of the segment L_A and its midpoint P_a in the 3-D model, and use the total station to measure the corresponding two of the corresponding positions on the building at the same position and corresponding to the segment L_B the position information of the endpoints B_1 , B_2 , and the midpoint P_b , then calculate $|A_1B_1|$, $|A_2B_2|$ and $|P_aP_b|$.

Randomly select n primitive lines in the façade of the building to calculate the distance difference, and find the average value as the distance offset c of the primitive line.

$$c = \frac{1}{3n} \sum_{i=1}^n (|A_1B_1| + |A_2B_2| + |P_aP_b|)_i \quad (9)$$

(2) Offset d of Angle

The line elements of the 3-D model constructed in 3-D space may be parallel, intersect, or disjoint with the line elements in the real-world. The angle between the two primitive lines is measured as the angular offset value d of the geometric model line element. Assume:

$$\begin{aligned} \overrightarrow{A_1A_2} &= (x_2 - x_1, y_2 - y_1, z_2 - z_1) = (x_a, y_a, z_a) \\ \overrightarrow{B_1B_2} &= (x_4 - x_3, y_4 - y_3, z_4 - z_3) = (x_b, y_b, z_b) \end{aligned} \quad (10)$$

Then the angle $\theta \in (0, 90^\circ]$ between L_A and L_B is:

$$\theta = \frac{x_a x_b + y_a y_b + z_a z_b}{\sqrt{x_a^2 + y_a^2 + z_a^2} \cdot \sqrt{x_b^2 + y_b^2 + z_b^2}} \quad (11)$$

Randomly select n primitive lines to obtain the average value of the angular offset d of the 3-D model primitive line:

$$d = \frac{1}{n} \sum_{i=1}^n \theta_i \quad (12)$$

3. Implementation

3.1 Experimental Area

The area of the experimental area is about $750 m^2$, and the building to be collected is a complex single building with a height of $45 m$. The terrain around the building is flat and empty. In this area, it is suitable for UAV to collect data in the air. The structure of the building is special, and the eaves have a more prominent part. The multi-angle view of the building is shown in Figure 3:



Fig. 3 Multi-view of the building

3.2 To Get Multi-Source Date

In the airborne area of the implementation, To use the Phantom 4 Pro camera of the DJI (Phantom 4 Pro V2.0) multi-rotor UAV continuously shoot the building by using the navigation method. The flying height was set to $80 m$, the heading overlap is set to 80% and the side overlap is set to 75% . Make sure that the direction of the route is as consistent as possible with the horizontal and vertical directions of the experimental area. At the same time, In order to ensure that the collected data has clear texture and complete data, To slow down the flight speed of the drone while making the area to be photographed wider, The resulted in 225 high-definition images with a pixel size of 4000×3000 .

The ground area uses a terrestrial LiDAR to acquire point cloud data around the building and the area where the UAV cannot get the data, to make up for the singularity and limitations of the UAV oblique photography technology, meanwhile, it can improve the authenticity and integrity of the 3-D real-world model. In this experiment, the Riegl VZ-1000 terrestrial laser scanner was used to collect the point cloud data. After surveying the site conditions of the building, and Select 8 scanning sites around the building to accurately scan the building. Figure 4 shows the data acquisition process:

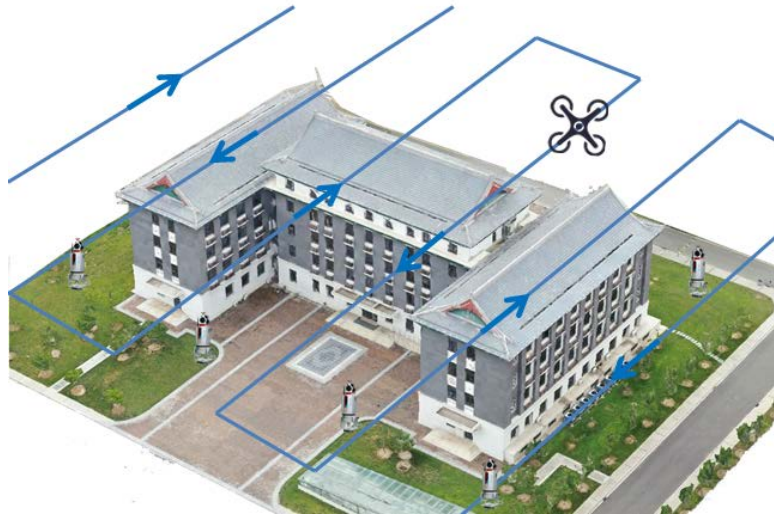


Fig. 4 Process of obtaining data

3.3 Modeling Based On Multi-Source Data Fusion

3.3.1 Data Preprocessing

First, to process the image data by aerial triangulation, after completing this step, check if the data is distorted. If the data is distorted, needing to continue processing the data by aerial triangulation. According to the requirements of the layout control point, a certain number of control points are added in the area. Then, to adjust the adjustment for the data that has been processed by bundle method. Taking the collinear equation of central projection as the basic equation of adjustment unit, through the rotation and translation of each ray beam in space, the common ray between models achieves the best intersection, and the whole region is added into the coordinate system of control points, thus restoring the object square position relationship between terrestrial objects. oblique images through aerial triangulation encryption is completed, can undertake the construction of 3-D model, through the high precision image matching algorithm [21], the model can automatically match the homonymous points in all images, and through screening and concise image point cloud to obtain the image of a sparse point cloud.

The laser point cloud data can be obtained through the terrestrial laser scanner, and the point cloud data can be stitched to obtain the complete point cloud model. After continuing to delete unrelated point clouds for the complete point cloud model, a high-precision 3-D laser point cloud can be obtained.

3.3.2 Point Cloud Fusion and Modeling

To registration and fusion the processed image point cloud and the laser point cloud. Since the accuracy of the 3-D laser point cloud is much higher than the accuracy of the image point cloud, the two point cloud data are registered and merged, and the 3-D laser point cloud is used as a reference. Firstly, by finding the feature points with the same name, to execution the point cloud coarse registration, and then this method can obtain complete point cloud results. In order to improve the overall accuracy of the point cloud registration, the point cloud is finely registered by using the ICP algorithm to obtain more accurate fusion point cloud model.

Need to build a high-precision 3D model after point cloud registration is completed. And the point cloud model obtained by the point cloud fusion is used to build Triangulation Irregular Network (TIN) by aerial triangulation. By setting the texture layers to "Multiply" in the layer blend mode dropdown, making to merge the colors and textures with the shading of the clay model base, Thereby generating a complete high-precision 3-D model. Figure 5 below is the construction process of the 3-D model.

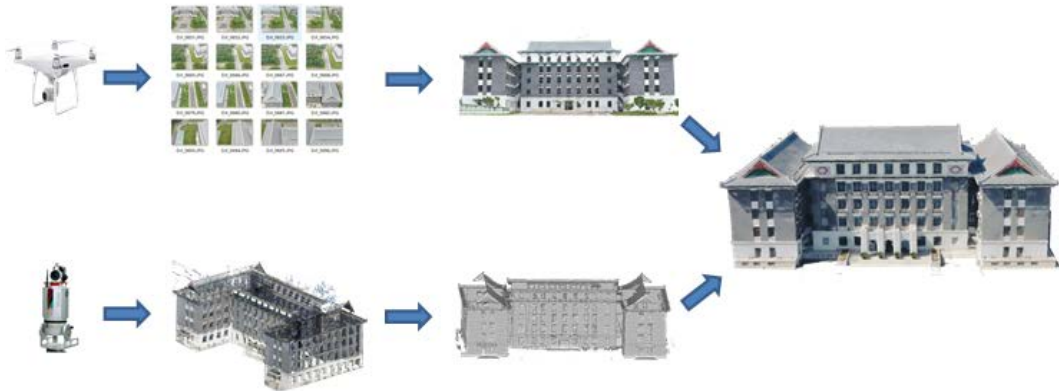
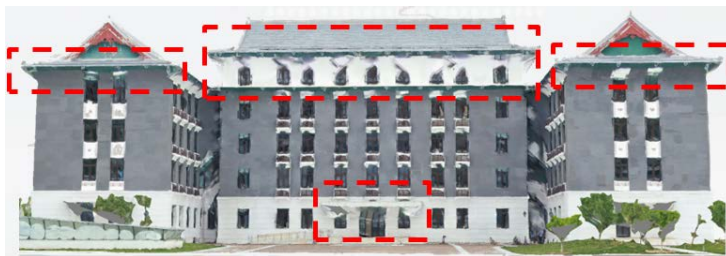


Fig. 5 Construction process of 3-D Model

4. Result Analysis

4.1 Visual accuracy assessment

In ideal conditions, the 3-D model should be consistent with the real building in the shape, size, etc. However, in the actual operation process, due to different methods of acquiring data and different methods of constructing the model, certain errors will inevitably occur. In order to verify and evaluate the geometric quality of 3-D modeling, through visual observation, to juxtapose 3-D model made by the three methods, as shown in Figure 6 below:



(a) UAV



(b) TLS



(c) UAV+TLS

Fig. 6 Comparison of model quality generated by different methods

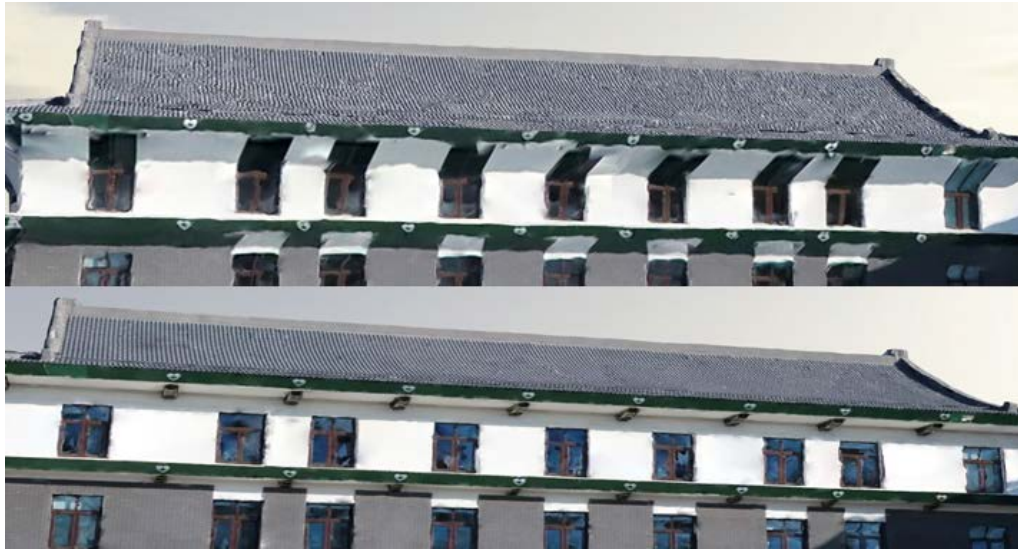


Fig. 7 Comparison of single data modeling and multi-source data modeling

As shown in Figure 6 above, it can be seen that the 3-D model texture constructed based on the UAV oblique photography technology has authenticity, and the modeling effect on the top of the building is better, but the data is less captured for the occluded part of the building (in the red box in Figure 6(a)), causing distortion of the part of the model. The 3-D model based on the terrestrial 3-D laser scanning technology can acquire more complete for the bottom point cloud data, the model has no distortion or void phenomenon. However, due to the limitations of the instrument itself, the top information of the building cannot be obtained (in the green box in Figure 6(b)).

It can be seen from the above Figure 7 that the wall surface is more flat in the 3-D model built by the multi-source data fusion modeling technology, the distortion at the bottom of the model is improved, and the overall effect is more real and complete, which makes up for the limitations of single technology modeling.

4.2 Accuracy evaluation based on primitive points and line

When the number of selected checkpoint n is 50, according to formula (3) and (4), a of the distance offset is calculated to be 1.5 cm . Meanwhile, randomly select 30 primitive lines on the outer surface of the building, according to formulas (9), and calculate the mean value c of the distance offset is 0.73 cm . because most of the buildings are regular shapes, the primitive lines are mostly horizontal and vertical, and the overall angular offset are small, According to formulas (10), (11) and (12), calculate the angular offset d value is only 0.48° .

Meanwhile, According to formulas (5) to (8), it can be seen from the data in Table 1 that the error in the plane of the 3-D real-world model constructed by multi-source data fusion is 0.058 m , and the error in the elevation is 0.038 m , in line with the accuracy requirements of the specification for Class I products, in practical production applications, in order to improve the integrity and authenticity of the 3-D model, a variety of data fusion modeling methods can be selected.

Table 1 Medium error of the fusion model

Fusion model	Number of checkpoints	X direction	Y direction	Mean square error of elevation	Flat error
	50	0.047m	0.035m	0.038m	0.058m

The 3-D real-world model based on multi-source data fusion realizes the omnidirectional restoration of the building, and improves the ability of visual representation of 3-D spatial data, and then it also broadens the application field of 3-D real-world model and promotes the further development of 3-D reconstruction technology. It provides a certain reference value for the digital expression of many fields.

5. Conclusions

With the acceleration of urban construction, there is a growing demand for spatial 3-D basic information. At the same time, as the basic data of 3-D space, the 3-D real-world model is widely used. Aiming at the deformation of the 3-D model caused by the data shadows originate in the oblique photography technology, this article uses a method of the terrestrial LiDAR combined with UAV oblique photogrammetry to reconstruct the 3-D model of the building. To registration coordinates and to merge point cloud data for acquired data, which makes up for the point cloud vulnerability caused by the blind spot limitation of the oblique photography due to the occlusion of the eaves. Through the accuracy analysis of the obtained model results, the mean square error of the constructed 3-D real-world model plane is 0.058 m , and mean square error in elevation is 0.038 m . Experiments show that the fusion of 3-D laser point cloud and image point cloud data improves the modeling effect of the 3-D model of oblique photogrammetry, making the modeling accuracy more reliable. Constructing high-precision 3-D building models and realizing building visualization can provide high-value basic information and sensory information for smart cities, and can improve the intelligence of smart city construction and contribute to the development of high-quality modern smart cities.

References

- 1) S. Kudva and X. Ye, Smart cities, big data, and sustainability union, Big Data and Cognitive Computing, vol. 1, no. 1, 2017.
- 2) J. L. Van Genderen, Airborne and terrestrial laser scanning, International Journal of Digital Earth, vol. 4, no. 2, pp. 183-184, 2011.
- 3) A. J. Cawood, C. E. Bond, J. A. Howell, R. W. H. Butler, and Y. Totake, LiDAR, UAV or compass-clinometer?
- 4) Accuracy, coverage and the effects on structural models, Journal of Structural Geology, vol. 98, pp. 67-82, 2017.
- 5) M. Lato, J. Kemeny, R. M. Harrap, and G. Bevan, Rock bench: establishing a common repository and standards for assessing rockmass characteristics using LiDAR and photogrammetry, Computers & Geosciences, vol. 50, pp. 106-114, 2013.
- 6) M. Koreň, M. Mokroš, and T. Bucha, Accuracy of tree diameter estimation from terrestrial laser scanning by circle-fitting methods, International Journal of Applied Earth Observation and Geo-information, vol. 63, pp. 122-128, 2017.

- 7) L. Javernick, J. Brasington, and B. Caruso, Modeling the topography of shallow braided rivers using structure-from-motion photogrammetry, *Geomorphology*, vol. 213, pp. 166-182, 2014.
- 8) J. Šašak, M. Gallay, J. Kaňuk, J. Hofierka, and J. Minár, Combined use of terrestrial laser scanning and UAV photogrammetry in mapping alpine terrain, *Remote Sensing*, vol. 11, no. 18, 2019.
- 9) F. Remondino, Heritage recording and 3d modeling with photogrammetry and 3D scanning, *Remote Sensing*, vol. 3, no. 6, pp. 1104-1138, 2011.
- 10) T. Tang, W. Zhao, H. Gong, A. Zhang, J. Pan, and Z. Liu, Terrestrial laser scan survey and 3D TIN model construction of urban buildings in a geospatial database, *Geocarto International*, vol. 23, no. 4, pp. 259-272, 2008.
- 11) E. Rupnik, F. Nex, and F. Remondino, Oblique multi-camera systems – orientation and dense matching issues, *ISPRS - International Archives of the Photogrammetry, Remote Sensing and Spatial Information Sciences*, vol. XL-3/W1, pp. 107-114, 2014.
- 12) L. Zhu, J. Hyypä, A. Kukko, H. Kaartinen, and R. Chen, Photorealistic building reconstruction from mobile laser scanning data, *Remote Sensing*, vol. 3, no. 7, pp. 1406-1426, 2011.
- 13) C. Sahin, A. Alkis, B. Ergun, S. Kulur, F. Batuk, and A. Kilic, Producing 3D city model with the combined photogrammetric and laser scanner data in the example of taksim cumhuriyet square, *Optics and Lasers in Engineering*, vol. 50, no. 12, pp. 1844-1853, 2012.
- 14) J. Balsa-Barreiro and D. Fritsch, Generation of visually aesthetic and detailed 3D models of historical cities by using laser scanning and digital photogrammetry, *Digital Applications in Archaeology and Cultural Heritage*, vol. 8, pp. 57-64, 2018.
- 15) S. Pu and G. Vosselman, Building facade reconstruction by fusing terrestrial laser points and images, *Sensors (Basel)*, vol. 9, no. 6, pp. 4525-42, 2009.
- 16) H. El-Din Fawzy, 3D laser scanning and close-range photogrammetry for buildings documentation: A hybrid technique towards a better accuracy, *Alexandria Engineering Journal*, vol. 58, no. 4, pp. 1191-1204, 2019.
- 17) Y. He, B. Liang, J. Yang, S. Li, and J. He, An iterative closest points algorithm for registration of 3D laser scanner point clouds with geometric features, *Sensors (Basel)*, vol. 17, no. 8, Aug 11 2017.
- 18) L. M. Belmonte, R. Morales, and A. Fernández-Caballero, Computer vision in autonomous unmanned aerial vehicles—A systematic mapping study, *Applied Sciences*, vol. 9, no. 15, 2019.

- 19) P. Anca, A. Calugaru, I. Alixandroae, and R. Nazarie, A workflow for UAV's integration into a geodesign platform, *ISPRS - International Archives of the Photogrammetry, Remote Sensing and Spatial Information Sciences*, vol. XLI-B1, pp. 1099-1103, 2016.
- 20) Chessa, S., Girolami, M., Mavilia, F., Dini, G., Perazzo, P., & Rasori, M, Sensing the cities with social-aware unmanned aerial vehicles, *Proceedings - IEEE Symposium on Computers and Communications*, 278–283, 2017.
- 21) X. Kang, J. Li, X. Fan, and W. Wan, Real-time RGB-D simultaneous localization and mapping guided by terrestrial LiDAR point cloud for indoor 3-D reconstruction and camera pose estimation, *Applied Sciences*, vol. 9, no. 16, 2019.
- 22) F. Remondino, M. G. Spera, E. Nocerino, F. Menna, and F. Nex, State of the art in high density image matching, *The Photogrammetric Record*, vol. 29, no. 146, pp. 144-166, 2014.

Development of Assistive Devices to Assist Daily Lives for People with Disability

Takakazu Ishimastau*, Motohiro Tanaka** and Jiangli Yu***

ABSTRACT: Nowadays quality of life (QOL) of people with disability is an important issue in our society. From the standpoint of engineering, we are requested to innovate the environment of the people with disability by introducing scientific technologies. There exist many commercialized assistive devices. But they are not enough to satisfy the various demands. In this paper many trials to develop assistive devices are shown responding the requests from people with disability. These developments could be achieved by many kinds of voluntary activities with the hot intention to assist people with disability.

1. Introduction

Due to the development of advanced science technologies, people with serious disabilities are now able to live with their families at home. As for the symptoms of intractable ALS disease, the muscle of the patient deteriorates, and limbs are paralyzed. In a couple of years after onset of the disease patients are obliged to wear artificial ventilator and becomes bed-ridden status. Furthermore, even the basic communication measure to utter voices becomes difficult. Total number to the ALS patients is estimated around 9,200 in Japan and around 70 in Nagasaki prefecture. In order to support their lives, various groups and association are working. Japan ALS association organized in 1986 is the biggest association to support ALS patients. The association aimed to investigate the cause of ALS and to develop the treatment methods of ALS. Development of assistive devices for ALS patient is also an important issue to support ALS patients. Current advanced assistive technologies enable serious ALS patients to communicate with care givers by using eyeball movements as shown in Fig.1, where eyeball movement can be detected by using an image sensor. Development of communication devices and environmental control devices enabled the patients to operate computers and mobile phone. And the quality of life of ALS patient is improving.

Using the assistive device, they write E-mail to friends and enjoy Web meeting. Even lots of assistive devices are developed, symptoms of patients are various. They requires original devices those are suitable to their physical and mental situations.

In order to cope with this problem for every patient, a voluntary group are now starting their activities. In this paper, activities to develop assistive devices for ALS and serious diseases are discussed.

* Professor, Nagasaki University, ishi@nagasaki-u.ac.jp

** Professor, Kurume technical college, tanamo@kurume-it.ac.jp

*** Jiangli Yu, Tamadec Co. Ltd., Japan, jiangli@gmail.com

2. Daily Problems from Person with Disability

Patients suffered from serious diseases have various problems to live their lives in their environments. In the followings, some of the problems reported by the patients and also the solutions are proposed

1) Development of rear stand mounted behind the wheelchair

A request of a patient of cerebral palsy was to develop an assistive device for his wife. In his daily life, he uses electric wheelchair. A problem is that his wife has a disability in her lower limbs. She often has a difficulty to walk following the electric wheelchair. Therefore, his request is to attach a foldable stand to the wheelchair. In Fig.1 a proposed stand with an electric wheelchair is shown which is mounted behind the wheelchair. The stand is supported by a caster type single wheel.



Fig.1 Electric Wheelchair with Rear Stand

2) Unlock system of the entrance hall for multiple dwelling house

An ALS patient requested us to develop an unlock system of the entrance hall for their multiple dwelling house. At the entrance hall of his multiple dwelling house the electric entrance door is locked. Visitors have to push the room numbers on the front panel at the entrance hall and ask the resident to unlock the electric entrance door. The problem is that the ALS resident in the room is unable to operate the unlock system because of his physical disability. Most important visitors are care givers they often come and care the ALS resident. One solution to answer this problem is to settle a human-like robot in the room with the resident. Required functions to the robot is to detect call signal from inter-phone and recognize the visit of care-givers and also to push the unlock button on the interphone. These functions can be simplified and installed on a simple device as shown in Fig.2. The device is composed of a microphone , a micro-computer (PIC16F88) and two motors. Procedures to unlock the entrance door are as follows:

- (a)Visitors push the call buttons at the entrance hall.
- (b)Assistive device detects the call sound by the visitor through the inter-phone.
- (c) Assistive device pushes the talk button and send beep sound signal to the visitor.
- (d) The visitor knocks at the microphone at the entrance hall along the procedure specified before.

(e) Assistive device acknowledges the knocking sounds from the entrance hall. If the sounds are emitted along the procedure specified before, the device unlock the door. Unless, the door remains locked.

The device was successfully settled to the resident room.

Recently, similar requests can be found since there exit many cases for serious patients to live alone at their house. Therefore, similar devices can be found in the shopping stores. Some of the device unlocks the door by the mobile phone.



Fig.3 Unlock system on the interphone

3) Smart environments for patient

We are requested to offer a smart environment to an ALS patient. A remaining ability of the patient is to move his fingers slightly. Fig.6 shows how the ALS patient control the environment by his fingers. He selects target items on the tablet as shown in Fig.8, where menus of electric appliances are shown. Fig.9 shows configuration of the smart environment.

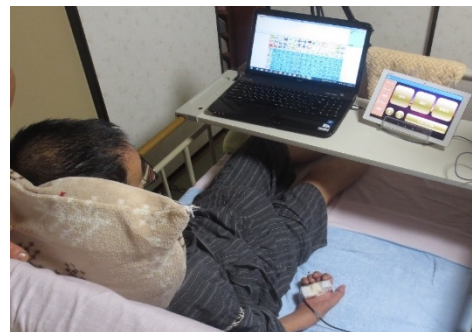


Fig.6 Patient and control tablet

In order to implement this system, the bed controller unit was developed as shown Fig.7 where four solenoid push mechanism were mounted on the four switches of the bed controller unit.

This smart environment assisted the ALS patient for one year.

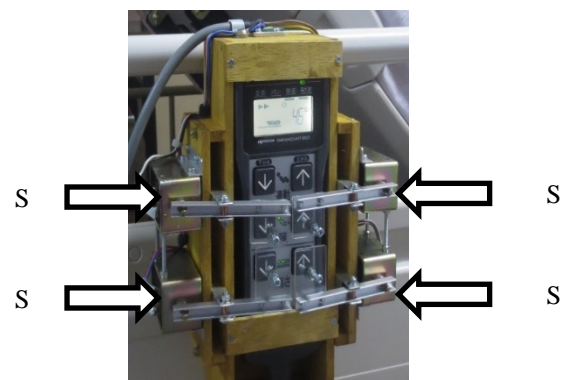


Fig.7 Bed controller unit with solenoid



Fig.8 Control tablet

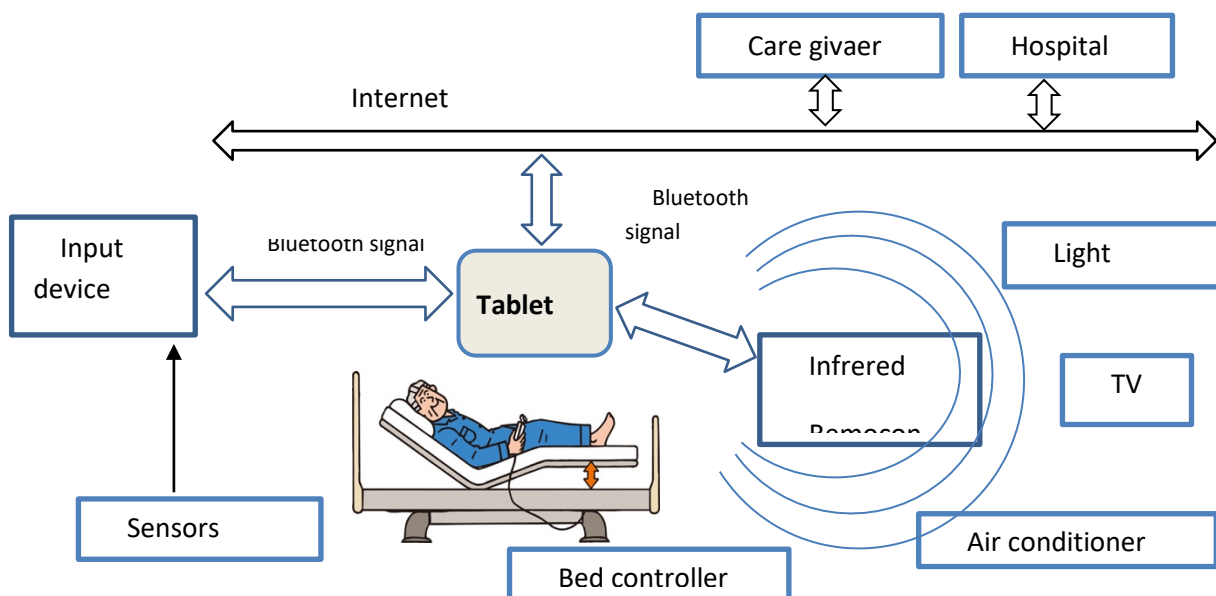


Fig.9 Smart environment for ALS patient

The operation of this smart environment system can be achieved just only touching one button on the controller watching the scanning bright cursor on the tablet. In this proposed smart environment, most important point is how to deal with the emergency case. In case the user has some serious troubles, what he has to do is to touch the button and keep touching for a couple of seconds. Then, an alert signal is sent to the care giver and hospital.

Fig.10 shows another smart environment system. The user on the bed is suffered by spinal cord injury. He can control his environmental devices like TV, air conditioning system, telephone, bed and also internet communication through the computer monitor on the ceiling.

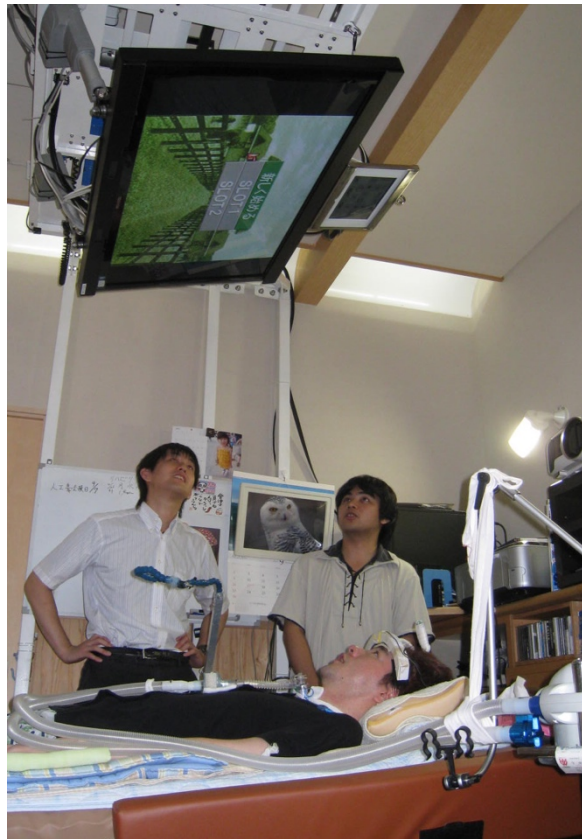


Fig.10 Smart environment for spinal cord injury

4) Development of communication device for spinal cord injury

The patient on the bed in Fig.10 is patient with spinal cord injury. He had an accident to fall down in the factory and damaged his spinal cord. His physical abilities below the neck was seriously damaged and four limbs were paralyzed. He needs artificial ventilator and could not utter voices. But physical abilities above the neck are in sound conditions. He can move neck, eyes, mouth as he wants. Considering his physical abilities, we offered an original computer communication device as shown in Fig.11. The patient wears a sensor band on his head. In this band a 2D acceleration sensor and a pressure sensor is mounted. 2D acceleration sensor is used to detect posture of the head. The 2D signal data is is used to move the computer cursor on the computer monitor. And the pressure sensor on the head band detects the chewing action of the user. This chewing action activates the click action like computer mouse click button. Therefore, this device is applicable to the communication device that enables the user to select desired character on the character table. The user can move the computer cursor at the desired position and select the character by chewing action. This device enabled fast operation of the computer.



Fig.11 Communication device to use head movement

3. Conclusions

In November, 2019 it was shocking news that an ALS patient requested medication to kill herself. Two doctors are arrested. After that many people are discussing about nursing issues for ALS patients and also people in the bed-ridden status. In Engineering department of Nagasaki university, projects to develop assistive devices for people with disability have been conducted for about 20 years. In this project, ALS is an important issue since the patient is physical disabled, but their intellectual function is totally normal. We developed many kinds of assistive devices and of course we offered the devices to ALS patient. But there exist many people with serious disability who need assistive devices those are suitable for their special physical features.

References:

- 1) Chao Zhang, Jiangle Yu, T. Ishimatsu: " Vision-based interface for people with serious spinal cord injury", Proceedings in 2015 IEEE SENSORS
- 2) Chao Zhang, Jiangle Yu, T. Ishimatsu: " An Environmental Control System for ALS Patient Using Finger Movement", Modern Mechanical Control ,Modern Mechanical Engineering, 5, 122-131 (2015)

VR Contents Development for Peace Education Class with Flight Yoke System and Headset

Byungdug Jun* and Norio Setozaki **

Abstract. In this research, we are trying to make an educational content for peace education. VR device and many tools such as flight yoke system and vive headset utilizing aircraft photos data. The aerial photographs were taken before and after the atomic bomb of Nagasaki. And the all created images clearly showed the situation and strength of the atomic bombing of Nagasaki in August 9, 1945. These contents were assumed that Japanese students and American students would be demonstration to the flight. We thought it was necessary to consider the global perspective of peace education. We hope to use in middle school class in Japan and America respectively.

Keywords: Peace Education, Hibakusha, VR Headset, Flight Yoke System

1 Introduction

During the 75 years after the World War II, the efforts of Japanese Hibakusha who is survivor for "peace activities and peace education" have given a desire of peace to the people all over the world. The origin of "ICAN" which won the Nobel Peace Prize in 2017 was a proof of "the activities of the hibakusha who were inspired by the scars of the war". However, recently in Japan, it was reported that a junior high school student on a school trip to Nagasaki was calling out to the storyteller of the peace guide, saying "He is a person who has escaped death or failed suicide" He who was junior high school student would not know the real WWII and does not understand its real image of the war. How we can teach them the truth of the war? They are called "digital generation" and "virtual generation". They will be main member for peace education and activities.

2 Tools and Contents

Until now, the analog peace action or educational activities by lectures and testimonies of the atomic bombings by Hibakusha are valuable experiences for the digital generation in the future. Digital and virtual which will be the main theme of peace educational activities for the new generation. What is the helpful method for virtual generation familiar with information terminals such as smartphones? It could be a place to practice a "new scheme of peace learning" that expands and use tools such as AR or VR which will be contents of peace and educational activities to the digital and virtual generation.

* Professor, Nagasaki University, bdjun@nagasaki-u.ac.jp

** Associate Professor, Nagasaki University, setozaki@nagasaki-u.ac.jp

In this research, we are focused on the succession of two scientific research funds (Grants-in-Aid for Scientific Research in Japan) so far. The new scheme of peace learning has following as three points. First one is that has the ability to make the new generation who has the negative legacy of war. Second one is that how we can make the global perspective (Japanese perspective, US perspective) for the contents of the global peace education. Third one is the importance of digital tools which are running on the mobile space familiar to them.

2.1 Flight Yoke System ¹⁾

The flight yoke system is for the fly commercial and private planes as a beginner or advanced pilot. The Logitech flight yoke system (see figure 1(a)) with included Throttle Quadrant features five total axes, stainless steel elevator and aileron control shaft, and 25 fully programmable buttons and switch positions. The yoke system is the hero of flight simulation and part of a complete, balanced setup all available, modular and interchangeable from Logitech G. We used this system for the simulator of peace education container with air photographs.

2.2 HTC Vive Virtual Reality Headset ²⁾

The Vive consists of a headset (see figure 1(b)), two controllers, and two infrared laser emitter units. The headset covers a nominal field of view of about 110 (approximately 90 per eye) through two 1080 x 1200 pixel displays that are updated at 90 Hz. As such, the Vive's pixel density is about 12 pixels, which means individual pixels can easily be seen when looking for them. This pixel density is similar to that of other current headsets and may limit the use of the Vive in psychophysical experiments. The Vive's tracker operates on a so-called inside-out principle, where no external cameras are needed. Instead, the Vive's tracking technology uses two laser emitters, called Lighthouses. These two boxes alternately send out horizontal and vertical infrared laser sweeps spanning 120 in each direction.

2.3 509th Composite Group and Photos by F-13

2.3.1 509th Composite Group ³⁾

The 509th Composite Group is one of the United States Army Air Forces. This unit dedicated to dropping the atomic bomb was established on August 11, 1943. Colonel Roscoe C. Wilson and Colonel Marvin C. Demler of the Army Air Force visited Los Alamos to launch an atomic bomb. It begins with a recommendation to immediately begin training combat units to drop. The new A-bomb drop squadron is due to complete the atomic bomb. It was very closely related to the time of atomic bomb. In the Manhattan Project, it was Colonel William S. Parsons of the Navy who led a group of scientists and made the atomic bomb usable in actual combat.



(a) Flight Yoke System by Logitech

(b) Vive Virtual Reality Headset by HTC

Figure 1 used two devices for peace education contents

In July 1944, the Colonel mentioned the training of the atomic bombing in a memorandum addressed to General Leslie R Groves, who was in charge of the Manhattan Project. Before using the atomic bomb in actual battles, it is necessary to conduct atomic bomb drop training by a dedicated unit in order to find out the initial defects of the newly built atomic bomb-equipped aircraft and solve various difficulties that occur in battle in advance.

Furthermore, since the Fatman-type atomic bomb can be easily changed to a high-performance bomb by simply refilling the inner shell with a high-performance explosive due to its structure, it is proposed to use a Fatman-type bomb for training. This will later be realized as an atomic bomb drop training by a simulated atomic bomb pumpkin.

On August 9 in 1945, a tropical cyclone occurred on the route passing through Ioshima, so they decided to avoid this route and sail directly to mainland Japan, and the meeting point between the atomic bomb carrier and the observation aircraft was over Yakushima in Kagoshima. It was not a sudden decision, but a default policy, that the bomb-based aircraft would be a boxcar operated by Charles W. Sweeney. There were 13 crew members in the A-bomb carrier-based boxcar. In addition to the regular crew of the Army Air Force, Commander Ashworth of the Navy, who could make the final decision regarding the dropping of the atomic bomb, was on board. The fact that the atomic bomb was dropped on Nagasaki is often seen in the message from Ashworth, who landed at Yomitan Airfield in Okinawa, to Brigadier General Farrell of Tinian.

The boxcar arrived over Yakushima, the meeting point, at the scheduled time, but failed to meet with the Hopkins plane and waited about 40 minutes (35 minutes according to Ashworth's record) before leaving for Kokura. They arrived at 9:44 over Himeshima, Oita Prefecture the starting point of the attack. Over the Kokura area, they couldn't shoot because of "haze and thick smoke", so they changed the course and took three bombing routes, but they could still not see the aiming point because of "haze and thick smoke". This is because the bomber Kermit K. Beahan could not see the designated target during the bombing itinerary over Kokura for the scheduled d-day. 50 minutes later, the second target, Nagasaki was chosen for the next main target instead of Kokura. After the war, in a sentence written by Ashworth⁵⁾, "We decided to attack the target and approached Nagasaki area with a radar due to the not good weather. And we dropped the last atomic bomb on Nagasaki area after observing for 30 seconds by visual inspection."

2.3.2 F-13 Aircraft for the Photos

Aircraft named F-13, the B-29 modified for photo reconnaissance was for the atomic bombing Hiroshima and Nagasaki. The crew of F-13 belonged to the 3rd Photo Reconnaissance Squadron, which was sometimes engraved as "3PRS" by taking the abbreviation. Members of the 3rd Photo Reconnaissance Squadron called themselves "Official Photographers of Japan". It means that Flying at high altitudes where the Japanese army's anti-aircraft fire did not reach, and it was difficult to intercept fighters. This describes the mission of continuing photo reconnaissance throughout the whole country freely. In May 1945, the 3rd Photo Reconnaissance Squadron became a unit with about 1000 members, including officers and non-commissioned officers. The first commander of the squadron was Lieutenant Colonel Patrick B. McCarthy.

Regarding the photo reconnaissance mission by the 3rd Photo Reconnaissance Squadron, the combat mission report of the squadron (Combat Mission) summarizes the route map and the operating status of the mounted camera for each operation.



Figure 2 Reconnaissance Aircraft named F-13 which has aircraft number (42-24853) of the Wright Airfield on October 6, 1944 ⁴⁾.

For operations after July 1945, all of the takeoff time, target, and return time to the base are described in Mariana's B-29 army unit, the daily report of the bomber group, and the operational summary. In addition to the combat mission report and operational summary, a photo reconnaissance investigation report (survey report) which analyzed the photographs obtained by the photo reconnaissance. It was prepared within a few days after the reconnaissance and was photographed.

Before and after dropping the atomic bomb on Nagasaki, the US military was recorded all over Nagasaki by air photos. Furthermore, the survey revealed that the aerial photograph records for reconnaissance purposes conducted before and after the atomic bombing were enormous. An aerial photograph of the sky over Nagasaki by a US military reconnaissance aircraft was released about four years after the publication of photographs before and after the atomic bombing of Hiroshima and it is now freely available to anyone. Figure 3 shows the image of aerial photographs before and after the atomic bomb.

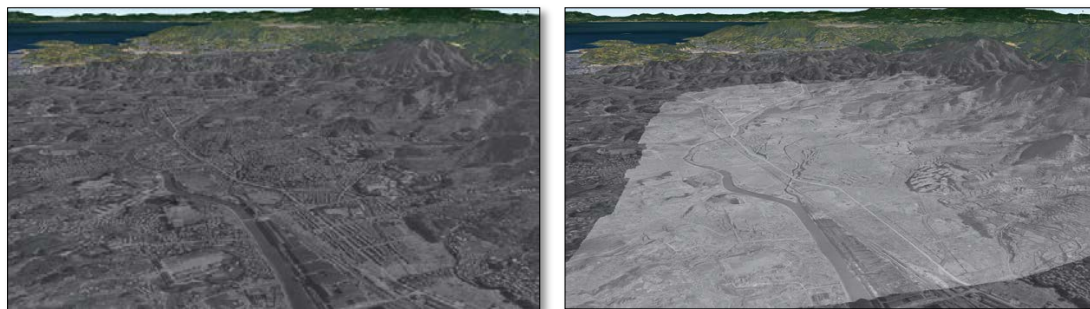


Figure 3 orthoimages of Aug. 7 before (left) and Sep. 7 after atomic bomb in 1945(right)



(a) headset image of starting point



(b) headset image of information viewing point



(c) flight scene of the pupil

Figure 4 HTC headset viewing image (a, b) and pilot scene of flight Learner(c)

3 Results and Discussion

Through this research, we were able to create VR content for peace education. In particular, aerial photographs were used to use the HTC Vive headset. The aerial photographs were taken before and after the atomic bomb of Nagasaki, and the images clearly showed the situation and strength of the atomic bombing. These contents were assumed that Japanese students and American students would be demonstration to the flight. We thought it was necessary to consider the global perspective of peace education. We are very much looking forward to the results from educational practice.

This work was supported by JSPS KAKENHI Grant Number 20K03255 and 20K12093.

REFERECES

1. <https://www.logitech.com/assets/65148/2/flight-yoke-system.pdf>
2. Diederick C. Niehorster, Li Li and Markus Lappe, The Accuracy and Precision of Position and Orientation Tracking in the HTC Vive Virtual Reality System for Scientific Reserch, i-Perception pp. 1-23, May-June 2017.
3. <https://www.afhra.af.mil/Information/Documents/>
4. Yozo Kudo and Tsutomu Kaneko, Atomic bombing troops - Atomic and pumpkin bombing by 509th composite group - , Omura Press Co. Ltd., 2013.
5. Ashworth f. L., The second atomic bombing – Nagasaki, Shipmate, pp. 18-22, 1987.



GISUP 2020, International